

UC Irvine

UC Irvine Previously Published Works

Title

Conditional Deletion of All Neurexins Defines Diversity of Essential Synaptic Organizer Functions for Neurexins

Permalink

<https://escholarship.org/uc/item/45q5s2kq>

Journal

Neuron, 94(3)

ISSN

0896-6273

Authors

Chen, Lulu Y
Jiang, Man
Zhang, Bo
[et al.](#)

Publication Date

2017-05-01

DOI

10.1016/j.neuron.2017.04.011

Peer reviewed



HHS Public Access

Author manuscript

Neuron. Author manuscript; available in PMC 2018 May 03.

Published in final edited form as:

Neuron. 2017 May 03; 94(3): 611–625.e4. doi:10.1016/j.neuron.2017.04.011.

Conditional Deletion of All Neurexins Defines Diversity of Essential Synaptic Organizer Functions for Neurexins

Lulu Y. Chen[§], Man Jiang[§], Bo Zhang, Ozgun Gokce[#], and Thomas C. Südhof^{*}

Department of Molecular and Cellular Physiology and Howard Hughes Medical Institute, Stanford University Medical School, 265 Campus Drive, Stanford, CA 94305, USA

Abstract

Neurexins are recognized as key organizers of synapses that are essential for normal brain function. However, it is unclear whether neurexins are fundamental building blocks of all synapses with similar overall functions, or context-dependent specifiers of synapse properties. To address this question, we produced triple conditional knockout mice that allow ablating all neurexin transcripts in mice. Using neuron-specific manipulations combined with immunocytochemistry, paired-recordings, and two-photon Ca^{2+} -imaging, we analyzed excitatory synapses formed by climbing fibers on Purkinje cells in cerebellum, and inhibitory synapses formed by parvalbumin- or by somatostatin-positive interneurons on pyramidal layer 5 neurons in the medial prefrontal cortex. After pan-neurexin deletions, we observed in these synapses severe but dramatically different phenotypes that ranged from major impairments in their distribution and function (climbing-fiber synapses) to large decreases in synapse numbers (parvalbumin-positive synapses) and severe alterations in action-potential-induced presynaptic Ca^{2+} -transients (somatostatin-positive synapses). Thus, neurexins primarily function as context-dependent specifiers of synapses.

eTOC Blurp

Using conditional deletions of all mouse neurexin genes, Chen et al. show that neurexins are key synaptic organizers that perform synapse-specific functions, ranging from synapse loss to impairments of synaptic transmission and a suppression of action potential-induced calcium influx.

^{*}Lead Contact tcs1@stanford.edu.

[§]These authors contributed equally

[#]Present address: Institute for Stroke and Dementia Research, Klinikum der Universität München, Ludwig-Maximilians-Universität LMU, München, Germany

Publisher's Disclaimer: This is a PDF file of an unedited manuscript that has been accepted for publication. As a service to our customers we are providing this early version of the manuscript. The manuscript will undergo copyediting, typesetting, and review of the resulting proof before it is published in its final citable form. Please note that during the production process errors may be discovered which could affect the content, and all legal disclaimers that apply to the journal pertain.

AUTHOR CONTRIBUTIONS

All authors designed and analyzed the experiments, L.C., M.J., B.Z., and O.G. conducted the experiments, and L.C., M.J., B.Z. and T.C.S. wrote the paper.

INTRODUCTION

Neurexins are presynaptic cell-adhesion molecules that were identified as α -latrotoxin receptors (Ushkaryov et al., 1992 and 1994). In vertebrates, neurexins are expressed in two principal forms, longer α -neurexins and shorter β -neurexins. α -Neurexins contain a large extracellular sequence comprising six LNS-domains (for laminin/neurexin/sex-specific globulin-domain) with three interspersed EGF-like domains, an O-linked carbohydrate attachment sequence, and a cysteine-loop domain (Fig. S1A). In α -neurexins, these extracellular sequences are followed by a single transmembrane region and a short cytoplasmic tail. β -Neurexins contain a short β -neurexin-specific N-terminal sequence that then splices into the α -neurexin sequence N-terminal to the last, sixth LNS-domain; from that point on, α - and β -neurexins are identical (Fig. S1A). Three vertebrate genes (*Nrxn1*, *Nrxn2*, and *Nrxn3* in mice) encode both α - and β -neurexins, with transcription of β -neurexins initiated by an internal promoter in the α -neurexin gene (Ushkaryov et al., 1993; Tabuchi and Südhof, 2002). α -Neurexins are evolutionarily conserved with one α -neurexin gene in *Drosophila* (Tabuchi and Südhof, 2002), and neurexin-related genes are identifiable throughout animals, including cnidaria that contain only a rudimentary nervous system (Ganot et al., 2016).

Neurexins are essential for multiple synaptic functions in *C. elegans*, *Drosophila*, mouse, and human neurons, but no uniform overall role for neurexins has emerged (Missler et al., 2003; Li et al., 2007; Etherton et al., 2009; Chen et al., 2010; Oswald et al., 2012; Aoto et al., 2013 and 2015; Anderson et al., 2015; Maro et al., 2015). Genetic mutations analyzed in various animals and different synapses uncovered diverse phenotypes that affect multiple aspects of synaptic function. In mice, constitutive single knockout (KO) of *Nrxn1 α* or *Nrxn3 α* with retained expression of β -neurexins severely impaired survival; triple KO of all α -neurexins was invariably lethal (Missler et al., 2003). Triple α -neurexin KO mice exhibited a decrease in inhibitory but not in excitatory synapse density, and displayed a dramatic impairment in excitatory and inhibitory synaptic transmission due, at least in part, to a loss in presynaptic Ca^{2+} -influx (Missler et al., 2003). Similarly, triple β -neurexin KO mice also exhibited a survival phenotype, albeit to a much milder one consistent with the relatively lower expression of β -neurexins than α -neurexins (Anderson et al., 2015; Fuccillo et al., 2015). Moreover, β -neurexin KO mice displayed a synaptic transmission impairment that was due, at least in part, to a disinhibition of tonic endocannabinoid signaling (Anderson et al., 2015). In terms of single neurexin gene deletions, only KOs of neurexin-1 α and of neurexin-3 $\alpha\beta$ have been analyzed in mice in detail (Etherton et al., 2009; Aoto et al., 2015). Most revealing of these analyses may have been the differential effect of neurexin-3 $\alpha\beta$ conditional KOs (cKOs) on excitatory synapses formed by hippocampal CA1-region neurons projecting to the subiculum, and inhibitory synapses formed by olfactory bulb granule cells contacting mitral cells (Aoto et al., 2015). In excitatory hippocampal synapses, the neurexin-3 $\alpha\beta$ deletion caused a selective trans-synaptic down-regulation of postsynaptic AMPA-type glutamate receptors (AMPA-Rs) without a change in presynaptic release. In inhibitory olfactory bulb synapses, however, the neurexin-3 $\alpha\beta$ deletion caused a selective decrease in presynaptic release without a change in postsynaptic receptor composition (Aoto et al., 2015). Thus, the same genetic manipulation of neurexin-3 $\alpha\beta$

produced different phenotypes depending on the type of neuron and synapse. A similar diversity of neuroligin functions has been described in *C. elegans* and *Drosophila* (Li et al., 2007; Chen et al., 2010; Oswald et al., 2012; Maro et al., 2015), suggesting that this may be a general feature of neuroligins.

A fascinating feature of neuroligins in vertebrates is their extensive alternative splicing that produces thousands of isoforms (Ullrich et al., 1995; Treutlein et al., 2015), but physiological evidence for the functional importance of neuroligin alternative splicing is available for only one site of alternative splicing in one neuroligin isoform, namely splice site #4 (SS#4) of neuroligin-3 (Aoto et al., 2013). Alternative splicing at this site, which is present in all α - and β -neuroligins, regulates *in vitro* binding of neuroligins to many of its ligands (neuroligins, dystroglycan, LRRTMs, cerebellins, and latrophilins; see Ichtchenko et al., 1995; Sugita et al., 2001; Boucard et al., 2005 and 2012; Chih et al., 2006; Uemura et al., 2010; Matuda and Yuzaki, 2011; Ko et al., 2009; de Wit et al., 2009; Siddiqui et al., 2010). Genetic manipulation of this splice site of neuroligin-3 in a manner that did not alter gene expression, but rendered all neuroligin-3 α and -3 β transcripts constitutively SS#4+ or SS#4- in a Cre-recombinase-dependent manner, revealed that presynaptic alternative splicing at SS#4 trans-synaptically regulates postsynaptic AMPARs in excitatory hippocampal synapses (Aoto et al., 2013). Moreover, these studies — which were performed *in vivo* enabled by the genetic manipulation — showed that presynaptic alternative splicing at SS#4 controls postsynaptic NMDA-receptor (NMDAR) dependent LTP, which also depends on AMPAR trafficking (Aoto et al., 2013). The regulated expression of other events of alternative splicing of neuroligins suggests that these events also mediate a profound control of synapses, but this has not yet been tested. If so, neuroligins may mediate a large number of pre- and trans-synaptic effects that shape synaptic transmission, and thereby control the neural circuits in which the various synapses reside.

The present data on neuroligins could be broadly explained by at least two hypotheses regarding their overall functions: (i) Neuroligins perform canonical shared functions regulated by alternative splicing, but exhibit differential patterns of redundancy owing to diverse co-expression of different neuroligin variants; or (ii) neuroligins perform different functions with limited redundancy, and the various functions are differentially activated in distinct synapses. The first hypothesis is supported by the observation of co-expression of diverse neuroligin variants in single neurons (Fuccillo et al., 2015) and the rescue of neuroligin-3 $\alpha\beta$ KO phenotypes by multiple neuroligin isoforms (Aoto et al., 2015), whereas no direct support for the second hypothesis is currently available. Nevertheless, we cannot at present conclude which hypothesis is correct because our understanding of neuroligins and their role in how synapses are formed and specified is hindered by several limitations. For example, the molecular interactions of individual neuroligins and their splice variants are incompletely understood. Apart from extracellular ligands for the 6th LNS domain that is shared by α - and β -neuroligins, only two extracellular ligands that bind to other α -neuroligin-specific sequences were identified (neuroliginophilins and dystroglycan), both of which bind to the 2nd LNS domain of α -neuroligins (Petrenko et al., 1996; Missler et al., 1998; Sugita et al., 2001). Likely other LNS-domains of α -neuroligins bind to additional ligands, but the nature of these ligands and the precise functions of any ligands are unknown. Moreover, the physiological roles of neuroligin-3 are only partly characterized, and even less is known about the functions

of neurexin-1 and neurexin-2. Furthermore, there is uncertainty about the redundancy between neurexins. As discussed above, the diversity of phenotypes produced by neurexin-3 $\alpha\beta$ cKOs in hippocampal and olfactory bulb synapses could be either due to differential redundancy among neurexins, or distinct synapse-specific functions of different neurexins.

In the current study, we aimed to specifically clarify whether neurexins perform canonical broad functions in all synapses, or synapse-specific functions that depend on the pre- and postsynaptic neuron type. For this purpose, we generated triple neurexin-1, -2, and -3 conditional KO (Nrnx123 cKO) mice that allow complete ablation of all neurexins by Cre-recombinase. We analyze the effect of the triple neurexin cKO on three different, well defined synapses, excitatory climbing-fiber synapses in the cerebellum and inhibitory synapses formed by parvalbumin-positive (Pv⁺) or somatostatin-positive (SST⁺) interneurons on layer 5 pyramidal neurons in the medial prefrontal cortex (mPFC). Our data reveal that each of the three synapses exhibits profound but different synaptic phenotypes after presynaptic deletion of all neurexins. In these experiments, all neurexins were deleted, excluding the possibility that a lack of a broad consistent phenotype is due to differential redundancy among neurexins. Thus, our results suggest that neurexins do not perform a series of canonical functions that are redundant among different neurexin genes, but instead perform distinct fundamental roles in different types of synapses.

RESULTS

Generation of triple neurexin-1, -2, and -3 (Nrnx123) cKO mice

The goal of the present study was to delineate the overall function of neurexins by examining the phenotype caused by deleting all neurexins. Because of the lethality of constitutive neurexin KO mice (Missler et al., 2003; Aoto et al., 2015), it was necessary to use conditionally mutant mice for an analysis of the deletion of all neurexins. We took advantage of neurexin-1, neurexin-2, and neurexin-3 cKO mice that we had generated for other projects, and that have either been published (Nrnx3; Aoto et al., 2015) or will be reported separately elsewhere (Nrnx1 and Nrnx2). In these mice, the first common exon shared by all α - and β -transcripts of each neurexin gene is flanked by loxP sites, enabling Cre-recombinase-dependent deletion of all of its α - and β -transcripts (Fig. S1A). We crossed individual α/β -neurexin cKO mice with each other for ~10 generations to generate homozygous triple Nrnx123 cKO mice that were viable and fertile. Expression of Cre-recombinase in hippocampal neurons cultured from triple Nrnx123 cKO mice showed that despite the need for recombination of six independent pairs of loxP sites for the complete deletion of all neurexins, this could be effectively achieved, resulting in a nearly total loss of neurexin-1, -2, and -3 expression (Fig. S1B).

In analyzing the effects of deleting all neurexins on neuronal and synaptic properties, we decided to focus on *in vivo* systems instead of cultured neurons. This choice was informed by the view that cultured neurons are suitable for uncovering fundamental cell-biological mechanisms as a reduced system, but do not replicate the *in vivo* development of synaptic specificity. To be able to examine specific types of synapses using parallel morphological and physiological approaches, we decided to study three defined types of synapses: (i)

excitatory climbing-fiber synapses formed by afferents from the inferior olive on cerebellar Purkinje cells, (ii) inhibitory basket-cell synapses formed on pyramidal neurons in layer 5 of the mPFC by Pv⁺ interneurons, and (iii) inhibitory synapses on apical dendrites formed on the same pyramidal neurons by SST⁺ interneurons (Fig. S2). In studying these three types of synapses, two of which contact the same postsynaptic cell, we hoped to not only examine neurexin function at specific defined synapses, but to also do this for a range of synapse types.

Sparse deletion of all neurexins from presynaptic climbing fibers in cerebellum

We injected lentiviruses expressing wild-type Cre-recombinase and double-floxed EGFP (test) or mutant Cre-recombinase (Cre) and mVenus (control) into the inferior olive of newborn (P0) Nrnx123 cKO mice, and analyzed the mice at P24, P35, and P45 (Fig. 1A–1C). The lentiviruses infected a subset of olivary neurons, resulting in sparse expression of EGFP or mVenus (which are encoded by the lentiviruses together with active or mutant Cre-recombinase) in a subset of climbing fibers that were identified in cerebellar cortex by virtue of their fluorescence (Fig. 1C, S2A).

We found that sparse deletion of neurexins caused a dramatic blunting of climbing fibers in the cerebellar cortex at P24, and a nearly complete loss of the corresponding climbing fibers at P35 and P45 (Fig. 1D–1G, S3A–C). At P24, neurexin-deficient fibers were no longer present in the extended dendritic tree of Purkinje cells but stopped abruptly at the layer of the Purkinje cells. Moreover, neurexin-deficient climbing fibers in the Purkinje cell layer contained no detectable synapses (Fig. S3A, B). In contrast, wild-type climbing fibers expressing GFP exhibited a normal distribution, extending into two-thirds of the molecular layer, and formed abundant synapses (Fig. 1D, S3A., S3B). At P35, only a few neurexin-deficient climbing fibers were detectable in cerebellar cortex, while at P45 no such fibers were observed (Fig. 1E, 1G). Since after lentiviral pan-neurexin deletions in the inferior olive most climbing fibers were from non-infected cells, the overall climbing-fiber synapse density (as measured by staining for the presynaptic marker vGluT2 that specifically labels climbing-fiber synapses) was normal in cerebellum at P24 (Fig. 1H, 1I, S3D).

Next, we patched in acute cerebellar slices Purkinje cells adjacent to labeled blunted neurexin-deficient climbing fibers, and measured synaptic responses elicited by climbing-fiber stimulation (Fig. 1J–1L, S3E; Zhang et al., 2015). We observed no change in climbing-fiber EPSC amplitudes, paired-pulse ratio, or kinetics, and also detected no change in synapse elimination as monitored by measurements of the ESPC size as a function of increasing stimulus strength (Fig. 1J–1L, S3E). These normal results likely reflect the normal innervation of Purkinje cells by climbing fibers from non-infected olivary neurons, suggesting that after sparse neurexin deletions, neurexin-deficient climbing fibers may not actively innervate Purkinje cells consistent with the synapse staining results.

Global neurexin deletion from all presynaptic climbing fibers in cerebellum

The most parsimonious explanation for the stunted growth and apparent inability to form synapses of neurexin-deficient climbing fibers after sparse deletions would be that these fibers are at a competitive disadvantage compared to excess wild-type climbing fibers,

leading to the elimination of the neurexin-deficient climbing fibers during the development of olivo-cerebellar synapses (Lorenzetto et al., 2009; Hashimoto et al., 2009). To test this hypothesis, we globally deleted neurexins in all inferior olive neurons using AAVs instead of lentiviruses (Fig. 2A–C, S2A). We then analyzed the distribution of climbing fibers and their synapses in cerebellar cortex.

We found that in the absence of surrounding wild-type climbing fibers, neurexin-deficient climbing fibers entered the molecular layer of the cerebellar cortex normally and were no longer blunted (Fig. 2D, 2E). However, neurexin-deficient climbing fibers extended less far into the molecular layer than wild-type climbing fibers, with a major loss of fibers at a distance of 70–80 μm from the PC layer (Fig. 2E). The density of climbing-fiber synapses as monitored by vGluT2 staining was normal in the zone proximal to Purkinje cells, but decreased in the zone more distal to Purkinje cells (Fig. 2F, S4A), thus correlating with the climbing fiber density. No apparent change in the density of the much more numerous parallel fiber synapses was detected (Fig. S4B, C). These data suggest that when neurexins are uniformly deleted from all climbing fibers, climbing fibers and their synapses exhibit an almost normal distribution.

To test whether the pan-neurexin deletion impairs climbing-fiber synaptic transmission as opposed to climbing-fiber synapse formation, we analyzed climbing-fiber synapses electrophysiologically in acute slices. Using standard recording conditions (-70 mV holding potential, with the high-affinity AMPA receptor antagonist NBQX [0.5 μM] to ensure voltage-clamp control given the large climbing-fiber EPSC amplitude, and with 2 mM Ca^{2+} in the medium), we observed a large decrease ($\sim 50\%$) in EPSC amplitude and a small increase ($\sim 15\%$) in paired-pulse ratio, consistent with a combination of a reduction in synapse numbers and a decrease in release probability (Fig. 2G, 2H, S4D). EPSC rise times were normal, while EPSC decay times were slightly shorter, possibly owing to the decrease in amplitude and the loss of distal synapses. In agreement with the lack of a major morphological change, single-fiber innervation of Purkinje cells was unaltered (Fig. S4D, S4E).

To further characterize neurexin-deficient climbing-fiber synapses, we repeated the synaptic recordings at a -10 mV holding potential, and added the competitive low-affinity AMPA-receptor antagonist γ -D-glutamylglycine (DGG, 2 mM) instead of NBQX. DGG was used because under standard conditions, the EPSC reflects release events per synapse, whereas the substitution of NBQX for DGG allows detection of glutamate concentration differences induced by the simultaneous release of single or multiple vesicles (Wadiche and Jahr, 2001). Under the DGG conditions, the pan-neurexin deletion caused a similar decrease in EPSC amplitude, but induced a significant decrease ($\sim 40\%$), as opposed to an increase, in paired-pulse ratio (Fig. 2I, 2J). We again observed no change in single-fiber innervation of Purkinje cells (Fig. S4G). These results suggest that the neurexin deletion not only decreases synaptic strength, but also alters the ratio of multi- to univesicular release at climbing-fiber synapses (Wadiche and Jahr, 2001).

Finally, we explored whether the neurexin deletion may trans-synaptically alter postsynaptic AMPA-receptor levels (Aoto et al., 2015) or other properties of quantal events, thereby

producing changes that could contribute to the observed decrease in synaptic transmission. To test this possibility, we measured synaptic transmission in the presence of Sr^{2+} instead of Ca^{2+} . Sr^{2+} can replace Ca^{2+} in triggering neurotransmitter release by binding to synaptotagmins, but is retained longer in the nerve terminal, thereby causing delayed quantal events that can be measured after an evoked EPSC (Fig. 2K). We found that just as in the presence of Ca^{2+} , the EPSC amplitude was massively decreased in the presence of Sr^{2+} , whereas the paired-pulse ratio was increased (Fig. 2L). Consistent with this result, the frequency of quantal events after the EPSC was also decreased, but the properties of quantal events were unchanged (Fig. 2M, S4G). These results suggest that postsynaptic AMPA-receptor levels and other quantal parameters are not changed by the pan-neurexin deletion.

Viewed together, these data confirm that neurexin-deficient climbing fibers form synapses that are weaker than wild-type synapses, thereby putting them at a competitive disadvantage if the surrounding synapses are from wild-type climbing fibers. The neurexin deletion appears to decrease synaptic strength primarily by lowering the release probability of the climbing-fiber synapses, with a concordant change in multivesicular release. Moreover, these data suggest that neurexins are not essential for synapse formation as such, but make essential contributions to the normal distribution, organization and function of climbing-fiber synapses. The relative loss of climbing-fiber synapses on distal Purkinje cell dendrites may be due to decreased competition of the weakened neurexin-deficient climbing fibers with normal parallel fibers.

Expression of neurexins, other synaptic cell-adhesion molecules, and marker genes in Pv^+ and SST^+ interneurons as analyzed by single-cell quantitative RT-PCR

In preparation to examining the role of neurexins in inhibitory synapses formed by Pv^+ and SST^+ interneurons on cortical pyramidal neurons, we compared their relative expression profiles using fluidigm-based single-cell quantitative RT-PCR. We identified Pv^+ and SST^+ interneurons in acute slices from Pv-Cre or SST-Cre mice that had been injected with AAVs expressing double-floxed eYFP at P21, and that were sacrificed at P35–P40. We patched the labeled neurons, aspirated cytosol, and performed mRNA measurement on the cytosol (Fig. S5). We found that apart from the typical markers for Pv^+ and SST^+ interneurons (such as parvalbumin, somatostatin, and synaptotagmin-2), both types of interneurons expressed similar overall levels of neurexins and of other synaptic cell-adhesion molecules (Fig. S5). *Lphn1* and *Slitrk3* exhibited significant differences between the two types of interneurons, but all three neurexin genes were expressed similarly.

Decreased numbers of inhibitory synapses formed by Pv^+ interneurons on pyramidal neurons in the mPFC

We crossed triple *Nrxn123* cKO mice with Pv-Cre mice that express Cre-recombinase under the parvalbumin promoter, and analyzed the density of synaptic puncta that were labeled with antibodies to parvalbumin or to vGAT in sections from the mPFC (Fig. 3A). We quantified the total density of puncta for each marker separately for the different cortical layers. Strikingly, we observed a dramatic decrease in the density and apparent area of Pv^+ and vGAT⁺ synaptic puncta in *Nrxn123* cKO/ Pv-Cre mice compared to littermate *Nrxn123* cKO mice (Fig. 3B, S6A–C). This loss was more pronounced for vGAT⁺ puncta (~50%)

than for Pv⁺ puncta (~25%), possibly because not all Pv⁺ puncta represent actual synapses. Indeed, quantifications of Pv⁺ puncta that are also vGAT⁺ revealed a decrease of ~60–70% (Fig. S6C). Thus, deletion of all neuexins from Pv⁺ interneurons leads to a loss of the majority of synapses formed by Pv⁺ interneurons.

To determine whether the remaining synapses formed by Pv⁺ interneurons are functional, we examined spontaneous miniature inhibitory postsynaptic currents (mIPSCs) in layer 5 pyramidal neurons of the mPFC, again comparing Nrnx123 cKO/Pv-Cre (test) with littermate Nrnx123 cKO mice at P35–P40 (control; Fig. 4A, 4B). We observed no change in mIPSC amplitude, but a 25% decrease in mIPSCs frequency that is consistent with the decrease in vGAT⁺ and Pv⁺ synapse density.

Next, for a specific analysis of the properties of synapses formed by Pv⁺ interneurons on pyramidal neurons, we performed paired recordings in acute slices from Pv-Cre/Nrnx123 cKO (test) and Pv-Cre mice (control). We stereotactically injected the mPFC of the mice with AAVs expressing double-floxed eYFP at P21, and analyzed the mice at P35–P40. Note that test and control slices for these experiments (and related experiments with SST⁺ interneurons described below) were not obtained from littermate mice, because the need for genetic labeling of Pv⁺ interneurons in order to perform paired recordings made that difficult (it would have required crossing a fifth genetic marker into the Nrnx123 cKO/Pv-Cre mice). Instead, the Pv-Cre control mice used in these experiments were generated from Nrnx123 cKO/Pv-Cre mice by crosses with wild-type mice of a similar genetic background. Control mice were separated less than 3 generations from Nrnx123 cKO/Pv-Cre mice, suggesting that they harbor a similar genetic background. Moreover, only age-matched control and test animals were used and were manipulated at the same time in parallel.

We patched adjacent Pv⁺ interneurons and pyramidal neurons, and confirmed the fast spiking properties of the Pv⁺ interneurons by current injections (Fig. 4C, 4D). We probed for synaptic connections by monitoring monosynaptic IPSCs (Fig. 4E). Despite the synapse loss, we observed that the success of establishing pairs during paired recordings was similar between the Nrnx123 cKO/Pv-Cre (52 successes/141 pairs tested (36.8%)) and Pv-Cre mice (32 successes/88 pairs tested (36.3%); Table S1). However, the IPSC amplitudes in Pv⁺ interneuron → pyramidal neuron synapses was decreased ~50% in Nrnx123 cKO/Pv-Cre mice compared to Pv-Cre mice (Fig. 4F), similar to the decrease in synapse density (Fig. 3). In neuexin-deficient Pv⁺ neurons, high-amplitude synaptic responses were preferentially lost, without a change in IPSC kinetics or in paired-pulse ratio, suggesting that decrease in IPSC amplitude is unlikely due to a change in release probability (Fig. 4F–4H). Overall, these experiments suggest that Pv⁺ interneurons in Nrnx123 cKO/Pv-Cre mice form synaptic connections of similar properties with the same number of postsynaptic pyramidal target neurons, but with fewer synapses per connection.

Next, we examined action-potential induced Ca²⁺-influx in Pv⁺ interneuron → pyramidal neuron synapses. We stereotactically injected the mPFC with AAVs expressing double-floxed mCherry at P21, and analyzed the mice at P35–P40. Pv⁺ interneurons in acute slices from Nrnx123 cKO/Pv-Cre and Pv-Cre mice were identified by expression of mCherry, and filled via the patch pipette with Alexa Fluor 594 (50 μM; Ca²⁺-insensitive dye to visualize

the axonal arbor) and Fluo-5F (200 μM ; Ca^{2+} -indicator to monitor presynaptic Ca^{2+} -transients), and imaged the filled neurons by two-photon microscopy (Fig. 5A). Analyses of the density of presynaptic boutons in the axonal arbors of Pv^+ interneurons revealed that the pan-neurexin deletion caused a significant decrease in bouton density ($\sim 25\%$), consistent with the decrease in synapse numbers (Fig. 5B). We confirmed by test-current injections that the patched neurons were fast spiking as characteristic for Pv^+ interneurons (Fig. 5C), and then measured presynaptic Ca^{2+} -transients as a function of presynaptic action potentials. Using this experimental configuration, we could reliably detect Ca^{2+} -transients in response to single action potentials, and detected a nearly linear relationship between the number of action potentials and Ca^{2+} -transients, measured as the Ca^{2+} -indicator signal in control neurons (Fig. 5D, 5E). We observed no change in the amplitude of the Ca^{2+} -transients as a function of action potentials or in the decay kinetics of the Ca^{2+} -transients upon presynaptic deletion of neurexins, consistent with the lack of a change in paired-pulse ratio. These experiments, viewed together, suggest that deletion of presynaptic neurexins from Pv^+ interneurons causes a discrete decrease in the density of synapses formed by these neurons on pyramidal neurons without a change in connectivity as such, or in the strength of these synapses.

Analysis of inhibitory synapses formed by SST^+ interneurons on pyramidal neurons in the mPFC

To test whether neurexins perform a similar function in another type of inhibitory synapse that differs from the synapses formed by Pv^+ interneurons, we analyzed synapses formed by SST^+ interneurons on the same class of pyramidal neurons in layer 5 of the mPFC. We used the same strategy as outlined above for Pv^+ interneurons, except that we employed SST-Cre mice instead of Pv-Cre mice (Fig. S1D). When we analyzed SST^+ or vGAT^+ synapses in cortical sections from littermate $\text{Nrnx123 cKO/SST-Cre}$ and Nrnx123 cKO mice, however, we detected no significant change in the density of SST^+ or vGAT^+ puncta, and only a small decrease in inhibitory synaptic puncta area as visualized by vGAT staining (Fig. 6, S7). Thus, eliminating all neurexins from SST^+ neurons does not appear to decrease the number of synapses formed by SST^+ neurons.

We next examined mIPSCs in $\text{Nrnx123 cKO/SST-Cre}$ and Nrnx123 cKO mice, but detected no change in frequency and amplitude (Fig. 7A, 7B). This result is not surprising, however, because SST^+ interneurons form synapses on distal dendrites of pyramidal neurons different from Pv^+ interneurons that form synapses on, or close to, the pyramidal neuron cell body. As a result, changes in mIPSCs mediated by SST^+ synapses would be hard to detect, given the massive attenuation of mIPSCs along the long distal dendrites.

We then performed paired recordings using virally labeled SST^+ interneurons, comparing $\text{Nrnx123 cKO/SST-Cre}$ mice with SST-Cre mice (Fig. 7C, 7D, Table S1). Importantly, the rate of successfully finding synaptically connected neurons was much lower in $\text{Nrnx123 cKO/SST-Cre}$ samples (7 connected pairs in 61 pairs tested (11.5%)) than in SST-Cre pairs (11 connected pairs in 43 pairs tested (25.6%)). Moreover, the synaptic connections that could be detected were much weaker after presynaptic deletion of neurexins, with a large decrease in mean IPSC amplitude ($\sim 40\%$). Strikingly, no SST^+ interneuron \rightarrow pyramidal

neuron synaptic connection exhibited an IPSC amplitude of >20 pA in *Nrxn123* cKO/SST-Cre mice, whereas >50% of these synapses exhibited IPSCs with amplitudes of >20 pA in SST-Cre mice (Fig. 7E, 7F). In addition, IPSCs elicited by stimulation of neurexin-deficient SST⁺ interneurons were much slower, as indicated by an increased synaptic latency (~30%) and increased rise time (~30%).

To test whether the decrease in synaptic strength in SST⁺ interneuron synapses is due to a decrease in release probability, we measured the paired-pulse ratio at SST⁺ interneuron → pyramidal neuron synapses. For this purpose, the extremely low synaptic strength of individual connections made it necessary to simultaneously stimulate multiple synaptic inputs from SST⁺ interneurons onto the same postsynaptic neuron. We achieved this by stereotactically infecting the mPFC of *Nrxn123* cKO/SST-Cre and SST-Cre mice at P21 with AAVs that contain double-floxed expression cassettes for a fusion protein composed of channelrhodopsin-2 and tdTomato. We then recorded IPSCs evoked by light stimulation from pyramidal neurons in layer 5 of the mPFC at P35–P40. The stimulation intensity was adjusted until a typical monosynaptic response with linear rise and exponential decay times were obtained; under these conditions, the first IPSC usually had an amplitude of 0.1–0.2 nA. Although this experimental setup does not allow measuring synaptic strength, it enables administering two closely spaced stimuli at defined intervals to monitor relative IPSC amplitudes during paired-pulse ratio measurements. Using this approach, we observed a large increase in paired-pulse ratios selective for short interstimulus intervals, consistent with a decrease in release probability (Fig. 7H).

We next asked whether the action-potential induced release from pan-neurexin-deficient SST⁺ interneurons is impaired because of a change in action-potential induced Ca²⁺-influx. For this purpose, we monitored the Ca²⁺-dynamics of presynaptic terminals in SST⁺ interneurons, using the same approach as described above for Pv⁺ interneurons. Again, Ca²⁺-transients induced by single action potentials could be reliably identified in individual presynaptic boutons (Fig. 8). Consistent with the lack of a change in synapse density, we detected no change in the density of presynaptic boutons as a result of the neurexin deletion (Fig. 8B). However, we observed that the neurexin deletion caused a large decrease in the amplitude of action-potential-induced Ca²⁺-transients. In control neurons, the Ca²⁺-transient increased almost linearly as a function of action potential numbers. In neurexin-deficient SST⁺ interneurons, the Ca²⁺-transient amplitude was uniformly decreased ~50%, and the Ca²⁺-transient decay time was significantly increased (Fig. 8D, E). These changes account for the decrease in release probability, suggesting that the neurexin deletion decreases synaptic strength in SST⁺ interneuron synapses at least in part by lowering Ca²⁺-influx.

DISCUSSION

Hundreds of studies attest to the importance of neurexins at synapses. These studies, broadly speaking, show that mutations or deletions of neurexins in organisms ranging from worms to humans cause synaptic dysfunction. Moreover, genetic studies in humans demonstrated that alterations in neurexin genes, in particular *NRXN1*, are associated with diverse neuropsychiatric disorders in a large number of patients. Considerable uncertainty reigns, however, about the precise role of neurexins at synapses. The functional consequences of

neurexin mutations differ dramatically between experimental preparations and various organisms, ranging from the original observation that deletions of all α -neurexins severely impair synaptic transmission (Missler et al., 2003), to more recent findings that neurexin-3 α / β deletions induce a loss of postsynaptic AMPARs at excitatory synapses in hippocampal neurons, but a decrease in the presynaptic release probability at inhibitory synapses in olfactory bulb neurons (Aoto et al., 2015).

Viewed together, the results from these earlier studies could be explained by at least two hypotheses about overall neurexin functions. First, different neurexin genes perform diverse but overall similar canonical functions in the fundamental organization of synapses, functions that are regulated by the various sites of alternative splicing of their mRNAs. As a result, deletions of different neurexins may produce distinct phenotypes in particular brain regions because a given neurexin variant exhibits different patterns of redundancy in various brain regions, depending on what other neurexin variants are co-expressed. According to this hypothesis that we originally favored (Aoto et al., 2015), neurexins perform a fundamental range of synaptic roles that can be differentially occluded in various types of synapses by redundancy via other neurexin isoforms. This hypothesis thus suggests that neurexins are basic building blocks of synaptic architecture and function.

As a second, alternative hypothesis, different neurexins perform diverse functions that may or may not be shared among neurexin isoforms, and that may differ among synapses. According to this hypothesis, neurexins are not central components of synaptic architecture, but act as essential modulators of an independent, canonical synaptic assembly machinery, adapting this machinery to the needs of a given synapse. This hypothesis envisions neurexins as a platform molecule whose diverse functions can be differentially activated by alternative splicing to confer specific properties to synapses, but which is not a central component of the basic design of synapses.

To distinguish between these two hypotheses, we tested the effect of deletions of all neurexins on synaptic transmission at distinct synapse types, with the notion that canonical neurexin functions, provided they exist, would become apparent by ablating all neurexin expression. Thus, our study provides a comprehensive attempt to examine the totality of neurexin functions in vertebrates. In order to achieve this goal, we had to generate homozygous triple cKO mice that allow conditional deletion of all neurexin isoforms constitutive deletions of neurexins is lethal (Missler et al., 2003; Fig. S1, S2).

Our data show that deletion of all neurexins produces dramatically different phenotypes in various types of synapses. Possibly most striking was the comparison of the effect of pan-neurexin deletions on P v^+ interneuron vs. SST $^+$ interneuron synapses formed on pyramidal neurons. Although these synapses are both inhibitory and target the same postsynaptic neurons, the pan-neurexin deletion decreased the number of P v^+ interneuron synapses without an apparent change in synaptic transmission in the remaining synapses (Fig. 3–5). In SST $^+$ interneuron synapses, in contrast, the pan-neurexin deletion maintained normal synapses numbers, but induced a massive impairment in action potential-induced Ca $^{2+}$ -influx, leading to a large decrease in release probability (Fig. 6–8). Thus, in these two types of synapses neurexins are selectively essential for different synapse parameters, arguing

against a canonical role of neurexins in all synapses and suggesting that neurexins perform different functions in different types of synapses, functions that seem to depend on the nature of the presynaptic neuron. Alternatively, it is conceivable that canonical neurexin functions are differentially compensated in various types of synapses by neurexin-independent pathways. Although we find this rather unlikely, this possibility is enabled by the chronic nature of our cortical manipulations, which provides time for distinct compensatory processes in different types of neurons. As a third, also unlikely possibility given the known properties and localization of neurexins, it is possible that the pan-neurexin deletions caused distinct phenotypes in different types of neurons because they impair a common upstream process that, however, is translated into different downstream consequences in various types of synapses. Future experiments studying specific neurexin functions in depth will have to address these questions.

The pan-neurexin deletion phenotypes we observed are interesting in their own rights. The effect of the sparse pan-neurexin deletion in climbing fibers (Fig. 1) most likely reflects an inability to compete with wild-type neighboring fibers (Hashimoto et al., 2003). The contrast between the massive phenotype detected upon sparse deletion of neurexins in climbing fiber synapses vs. the less pervasive phenotype observed upon global deletion of neurexins in the same synapses (Fig. 2) illustrates the role of competition in synapse formation in cases where there is a one-to-one relationship between pre- and postsynaptic neurons. Such competition, however, does not appear to explain the synapse loss observed in pan-neurexin-deficient P_v⁺-interneurons (Fig. 3). Here, the normal connectivity measured by the success rate of finding pairs, the fact that in paired recordings IPSCs and synapse numbers are decreased similarly (Fig. 4), and the observation that Ca²⁺-dynamics are normal (Fig. 5) favor the interpretation that the remaining synapses are functional and that neurexins control the number of synaptic connections, but not synaptogenesis as such or synaptic transmission in these synapses. Conversely, synapses formed by SST⁺ interneurons are severely impaired functionally — which accounts for the decreased rate of finding pairs — but synapse numbers are not (Fig. 6–8). The functional impairment of the SST⁺ interneuron synapses reveals an essential role for neurexins in enabling the localization of Ca²⁺-channels at synaptic release sites, as described originally for the triple α -neurexin KO mice (Missler et al., 2003). This phenotype does not necessarily imply a direct role of neurexins in Ca²⁺-channel recruitment, a role performed by RIMs and RIM-BPs (Kaeser et al., 2011; Acuna et al., 2016), but suggests a specific feature of neurexin function of SST⁺-interneuron synapses. This phenotype may, at least in part, reflect a delayed maturation of these synapses as reflected in the decreased Ca²⁺-clearance from the terminals after an action-potential burst (Jiang et al., 2015). It is striking that none of the three pan-neurexin KO phenotypes described here seems identical to the two neurexin-3 cKO phenotypes we previously identified in other synapses (Aoto et al., 2015), suggesting that we would probably discover a much larger range of phenotypes if we examined other types of synapses.

Like those of all studies, our results have several limitations that should be noted. First, if different neurexins do not perform the same canonical but diverse and distinct functions at a given synapse, despite their high degree of homology, we would only see the net sum of these functions after pan-neurexin deletions. Thus, the apparent phenotype of the triple neurexin deletion may be milder than that of individual neurexin deletions. Second, although

we showed that some functional synapses are produced in the three synapse types examined, other synapses and synaptic properties that we did not investigate may be more severely affected; naturally, we can only assess those functions that we directly tested. Third, we have not examined the mechanisms involved in the phenotypes, and cannot at present speculate on the molecular basis for the very different pan-neurexin KO phenotypes. Here, future structure-function studies will be illuminative.

Based on our findings, what do neurexins ‘do’? If we had only studied SST⁺ interneuron synapses, we would have concluded that consistent with the triple α -neurexin KO analysis, neurexins couple Ca²⁺-channels to synapses (Missler et al., 2003). Conversely, if we had only studied P_v⁺ interneuron synapses, we would have postulated a synapse-formation or synapse-maintenance function. The phenotypes are too severe in each type of synapse to refer to them as modulatory, and are too different between different types of synapses to be assigned to a similar basic mechanism. To clarify this conundrum, a molecular dissection of the function of each neurexin in different types of synapse will likely be required, which will then allow relating the particular molecular mechanism involved to the general design of synapses. Stay tuned!

STAR METHODS

Detailed methods are provided in the online version of this paper and include the following:

CONTACT FOR REAGENT AND RESOURCE SHARING

Further information and requests for resources and reagents should be directed to and will be fulfilled by the Lead Contact, Thomas C. Südhof (tcs1@stanford.edu)

EXPERIMENTAL MODEL AND SUBJECT DETAILS

The use and care of animals complied with the guidelines of Administrative Panel on Laboratory Animal Care at Stanford University. Triple floxed α/β -Nr_{xn}1, 2, 3 mice (Nr_{xn}123^{f/f}) were generated by flanking exon 18 with FloxP site (See Figure S1 for details). P_v-IRES-Cre and SST-IRES-Cre driver line were crossed with Nr_{xn}123^{f/f} mice to generate interneuron-specific Nr_{xn}123 knockout. Mice were maintained in the BL6/C57; CD1 mixed background. Breeding cages are maintained with crossing P_v-Cre/+; Nr_{xn}123^{f/f} and Nr_{xn}123^{f/f} or SST-Cre/+;Nr_{xn}123^{f/f} and Nr_{xn}123^{f/f}, respectively. Because it is difficult to precisely identify P_v⁺ and SST⁺ cells from Nr_{xn}123^{f/f}, we use P_v-Cre and SST-Cre mouse line without Nr_{xn}123^{f/f} as control in paired recording and calcium imaging experiments. All other experiments use littermate control without Cre expression.

The following primer sequences were used for genotyping:

Nr_{xn}1 flox: 5′ GTAGCCTGTTTACTGCAGTTCATTCC 3′

5′ CAAGCACAGGATGTAATGGCCTTTC 3′

Nr_{xn}2 flox: 5′ CAGGGTAGGGTGTGGAATGAGGTC 3′

5′ GTTGAGCCTCACATCCCATTGTCT 3′

Nrxn3 flox: 5' AATAGCAGAGGGGTGTGACAC 3'

5' CGTGGGGTATTTACGGATGAG 3'

Cre: 5' GAACCTGATGGACATGTTTCAGG 3'

5' AGTGC GTTCGAACGCTAGAGCCTGT 3'

1. Cerebellum: mice (male and female) were stereotactically injected at postnatal day (P) 0, then used for slice electrophysiology or immunohistochemistry experiments at P24.
2. Prefrontal cortex: mice (male and female) were stereotactically injected at P21, then used for slice electrophysiology or immunohistochemistry experiments at P35–40.

METHOD DETAILS

Stereotactic Injection of Viruses—Lentiviruses and AAVs were produced as described (Xu et al, 2013). For injection into the cerebellum, lentiviruses and AAVs were stereotactically injected into the inferior olive at P0 with home-made stereotactic platform. Injection sites were confirmed after the experiments by sectioning the inferior olive.

2. Prefrontal cortex: AAV expressing Ef1 α -DIO-eYFP (AAV-DJ), Ef1 α -DIO-mCherry (AAV5) and CAG-DIO-ChR2-tdTomato (AAV-DJ) were produced and stereotactically injected into the mPFC region at P21 (coordinates: 2.0 mm anterior to bregma; 0.4 mm lateral to midline; depth of ~2.1 mm from the dura, with 0.5 μ l AAV injected at 0.2 μ l/min with a microinjection pump).

Single-Cell Transcriptional Profiling—Single-Cell Transcriptional Profiling was performed as previously described (Fuccillo, et al., 2015). Briefly acute brain slices were cut as described above, and patch pipettes were used for cytosol extraction. Samples then underwent reverse transcription and target-specific amplification. Pre-amplified cDNAs were then processed for real-time PCR analysis on Biomark 96:96 Dynamic Array according to manufacturer's protocol (Fluidigm, USA). FAM-dye coupled detection assays were purchased from Integrated DNA Technologies (IDT, USA). To ensure the specificity of the amplification, all assays were tested with dilutions of mouse hippocampal cDNA to verify high efficiency (90–110%) and linear amplification ($R^2 > 0.96$) in every experiment. Expression values were calculated relative to average of ACTB and syt1 assays. Assays used the following primer sequences:

Sequences for the forward primer, internal probe and reverse primer for assays used in our single-cell analysis. Blank fields are displayed for pre-designed q-PCR assays purchased from IDT.

Electrophysiology and 2-photon Ca²⁺-imaging

Slice electrophysiology

1. Cerebellum: Sagittal slices (250 μ m thick) of the cerebellum were sectioned by standard procedures with a vibratome (LEICA VT1200S), using mice at age P24–26 after virus

injection at PO, similar as described previously (Zhang et al., 2015). Cutting solutions containing (in mM): 125 NaCl, 25 NaHCO₃, 2.5 KCl, 1.25 NaH₂PO₄, 25 glucose, 0.4 ascorbic acid, 3 myo-inositol, 2 Na-pyruvate, 0.1 CaCl₂ and 3 MgCl₂ (pH 7.4, when bubbled with 95% O₂/5% CO₂). The recording solutions containing (in mM): 125 NaCl, 25 NaHCO₃, 2.5 KCl, 1.25 NaH₂PO₄, 25 glucose, 0.4 ascorbic acid, 3 myo-inositol, 2 Na-pyruvate, 2 CaCl₂ and 1 MgCl₂ (pH 7.4, when bubbled with 95% O₂/5% CO₂). For the recordings of CF-EPSCs, picrotoxin (50 μM), strychnine (2 μM), NBQX (500 nM), and APV (50 μM) added to the extracellular solution. Internal solutions in pipette including (in mM): 140 Cs-gluconate, 20 TEA, 10 HEPES, 5 Na₂-phosphocreatine, 4 MgATP, 0.3 Na₂GTP, 5 Cs-EGTA, 0.1 Spermine, pH 7.2. Whole-cell recordings in the voltage-clamp mode were made with an Axon amplifier, under visualization of neurons with an upright microscope (BX51WI, Olympus,) equipped with a 40X water immersion objective (Zeiss). Patch pipette had resistances of 2–3 MΩ, and the series resistance (8–9 MΩ) was comparable between genotypes and was not compensated. Climbing-fiber mediated EPSCs were evoked using a bipolar stimulator and placed in the granule cell layer to evoked all-or-non response. The low-affinity competitive antagonist γ-D-glutamylglycine (γ-DGG; 2 mM) was included in aCSF with cell holding potential at –10 mV. Climbing-fiber synapse quantal recordings in Sr²⁺ were performed with 2 mM SrCl₂, 1 mM MgCl₂ in the aCSF instead of 2 mM CaCl₂, 1 mM MgCl₂. Stimuli consisted of paired pulses (10–40 V; 20 us duration) separated by 50 ms. Paired-pulse ratio (PPR) of evoked EPSCs was determined by dividing the amplitude of the second EPSC by that of the first.

2. Prefrontal cortex (PFC): All experiments were performed at P35–40. Coronal medial PFC slices were cut in a solution containing (in mM): 228 sucrose, 26 NaHCO₃, 11 glucose, 2.5 KCl, 1 NaH₂PO₄, 7 MgSO₄ and 0.5 CaCl₂, and recovered in artificial cerebrospinal fluid (aCSF) containing (in mM): 119 NaCl, 26 NaHCO₃, 11 glucose, 2.5 KCl, 1 NaH₂PO₄, 1.3 MgSO₄ and 2.5 CaCl₂. Whole-cell recordings were made from presynaptic interneurons using a K-gluconate based internal solution containing (in mM): 143 K-gluconate, 10 HEPES, 0.25 EGTA, 2 MgATP, 0.3 Na₃GTP, 7 phosphocreatine (pH 7.25–7.3; osmolarity 294–298) and from postsynaptic pyramidal cells using an CsCl-based internal solution containing (in mM): 75 CsCl, 68 K-gluconate, 10 HEPES, 0.25 EGTA, 2 MgATP, 0.3 Na₃GTP, 7 phosphocreatine (pH 7.25–7.3; osmolarity 294–298). With this CsCl-based solution, the theoretical reversal potential for Cl[–] was –14 mV, and IPSCs were inward currents at –70 mV. The impedance of patch pipettes was about 3–5 MΩ. Miniature IPSCs (mIPSC) was recorded in pyramidal cells in presence of 1 μM TTX, 20 μM CNQX and 50 μM D-APV.

For paired recording experiments, PV⁺ and SST⁺ interneurons were identified using green fluorescence expressed by AAV-DJ (Eflα-DIO-eYFP). Interneurons in Layer 5 were recorded at current-clamp mode by using K-gluconate based internal solution, and firing pattern was tested by step current injection (–100 to 800 pA). Paired recordings were recorded in PV⁺ or SST⁺ interneurons (in current-clamp mode) and nearby connected pyramidal (Pyr) cells (in voltage-clamp mode, ~50–100 μm away) by using CsCl based internal solution. Single AP were evoked by injecting current pulses (2 nA, 1 ms). All experiments were made at 32°C, using a Multiclamp 700B amplifier (Molecular Devices,

LLC). Voltage and current signals were filtered at 10 kHz and sampled at 20 kHz with Digidata 1440 (Molecular Devices, LLC). In PPR experiments in SST cell-Pyr pairs, we utilized optogenetics to simultaneously activate many synaptic inputs from SST+ cells by expressing CAG-DIO-ChR2-tdTomato virus. Specifically, CAG-DIO-ChR2-tdtomato (0.5 μ l for each hemisphere with a titer of $\sim 5 \times 10^{12}$) was injected into mPFC of Nrxn123 cKO/SST-Cre or SST-Cre mice at P21; as a result, ChR2 is only expressed in SST cells in the mPFC. Pyramidal cell responses to light pulse (0.05 ms, 10–20 mW) were recorded at P35–40. Because ChR2 always evokes complex responses (serrated responses with very different rise time/decay time), the laser intensity was adjusted until a typical monosynaptic response with clear linear rise times and exponential decays was obtained. The amplitude of the first IPSC was usually 100–200 pA, but is obviously dependent on viral expression and light intensity, and cannot be reproducibly quantified. However, paired pulses with different interstimulus intervals could be reliably measured, and the PPR was calculated from such experiments and compared by t-test one by one.

Ca²⁺-imaging was performed with a custom-built laser-scanning system based on an Olympus BX61WI microscope (Guo et al., 2015). Two-photon excitation was achieved with a mode-locked Ti:S laser (Chameleon Vision II, Coherent) running at a wavelength of 830 nm (repetition rate: 80 MHz; pulse width: 140 fs). Pv and SST interneurons were identified by expression of mCherry from AAV5-Ef1 α -DIO-mCherry. We recorded Pv+ and SST+ interneurons with a pipette solution similar to that of paired recordings (K-gluconate based internal solution) but without any additional Ca²⁺-buffer. We utilized Fluo-5F (200 μ M) as a Ca²⁺-indicator to monitor Ca²⁺ changes. Alexa Fluor 594 (50 μ M) was added into the internal solution for visualization of the cell morphology. The loading of Ca²⁺ indicator took about 20 minutes; Ca²⁺ transients could be then measured. We identified the axons of Pv and SST cells by their small diameter, randomly curved collaterals with densely distributed boutons. Axonal terminals were imaged with 5 or 10 \times digital zoom. APs were elicited by somatic injection of current pulses (1 ms, 2 nA) at 200 Hz. The number of APs varied from 1 to 20. Fluorescence changes were monitored in line scan mode. An individual sweep of line scan took 2 ms, and a trail of scan contained 1500 repeats. For each bouton and stimulus intensity, the fluorescent signals from 5 trials were averaged to increase the signal/noise ratio. Imaging data were acquired and further analyzed by using MATLAB (MathWorks). Ca²⁺-transients were presented by G/G_{max} calculated from the following equation: $G/G_{max} = \{G/R\}/\{G_{max}/R\}$ (G_{max} is the intensity of 200 μ M Fluo-5F in presence of 50 mM Ca²⁺ in ACSF, and R is the intensity of 50 μ M Alexa Fluor 594).

Immunohistochemistry—Immunohistochemical experiments were performed as previously described. Briefly, mice (~P24–P26 or ~P35–40) were anesthetized with isoflurane, perfused with phosphate-buffered saline (PBS) followed by 4% paraformaldehyde (PFA) in 0.1 M PBS via a perfusion pump (2 ml/min). Perfused brains were postfixed in 4% PFA for 2 h at room temperature (RT) and then cryoprotected in 30% sucrose (in 1X PBS) for 24 h at 4°C. Sagittal cerebellar slices or coronal mPFC slices (40 μ m) were cryo-sectioned at –20°C (Leica CM1050). Sections were serially washed with PBS and incubated in blocking solution (0.3% Triton X-100 and 5% goat serum in PBS) for 1 h at RT and incubated for 24 h at 4°C with primary antibodies diluted in blocking solution

(guinea pig anti-vGluT2, 1:500; mouse anti-Calbindin, 1:4000; rabbit anti-vGAT, 1:500; rabbit anti-Pv, 1:2000; rat anti-SST, 1:1000). Sections were washed four times (15 min each time) in PBS, treated with secondary antibodies (1:1000, Invitrogen, Alexa 488, Alexa 546, or Alexa 633) at 4°C overnight and washed four times (15 min each time) again in PBS. Sections were then mounted on superfrost slides and covered with mounting media (Vectashield, Vector Labs). Single plane images (at 1024 × 1024 resolution) from cerebellar lobules IV/V (areas of sulci excluded) or all layers (L1, L2/3, L5 and L6) of mPFC region were acquired using a Nikon confocal microscope (A1Rsi) with a 60X oil objective (PlanApo, NA1.4). All acquisition parameters were kept constant among different conditions within experiments. On average, 12 images from 4 brain sections were collected from each brain region or layers of each animal (N>3 animals per genotype/condition). For each experiment > 28 images per condition were collected and analyzed (mean ± SEM). Image backgrounds were normalized, and immunoreactive elements were analyzed with the Nikon analysis software. All unbiased automatic analyses were done from blinded groups.

QUANTIFICATIONS AND STATISTICAL ANALYSIS

All data are means ± SEM; numbers of neurons, sections, or ROIs/mice analyzed are shown in the bars or plots. Inter-group comparisons were done by two-tailed Student's *t*-test; (bar diagrams) or Kolmogorov-Smirnov test (cumulative distributions), multiple comparisons were analyzed with one-way ANOVA with Bonferroni's post-test (**p*<0.05, ***p*<0.01, and ****p*<0.001). Image backgrounds were normalized, and immunoreactive elements were analyzed with the Nikon analysis software. Test and controls were analyzed on anonymized samples to prevent observer bias.

Supplementary Material

Refer to Web version on PubMed Central for supplementary material.

Acknowledgments

We thank L. Chen, R. L. Zhong, Y. Wu, S. E. Hoffman and M. E. Simanski for help with the experiments and analyses. This study was supported by grants from the NIMH (MH052804 to T.C.S.) and the Simons Foundation (307762 to T.C.S.), and by a fellowship from the NIMH (F32MH100745 to L.Y.C.).

References

- Acuna C, Liu X, Südhof TC. How to Make an Active Zone: Unexpected Universal Functional Redundancy between RIMs and RIM-BPs. *Neuron*. 2016; 91:792–807. [PubMed: 27537484]
- Anderson GR, Aoto J, Tabuchi K, Földy C, Covy J, Yee AX, Wu D, Lee SJ, Chen L, Malenka RC, Südhof TC. β -Neurexins Control Neural Circuits by Regulating Synaptic Endocannabinoid Signaling. *Cell*. 2015; 162:593–606. [PubMed: 26213384]
- Aoto J, Martinelli DC, Malenka RC, Tabuchi K, Südhof TC. Presynaptic neurexin-3 alternative splicing trans-synaptically controls postsynaptic AMPA receptor trafficking. *Cell*. 2013; 154:75–88. [PubMed: 23827676]
- Aoto J, Földy C, Ilcus SM, Tabuchi K, Südhof TC. Distinct circuit-dependent functions of presynaptic neurexin-3 at GABAergic and glutamatergic synapses. *Nat Neurosci*. 2015; 18:997–1007. [PubMed: 26030848]

- Boucard AA, Chubykin AA, Comoletti D, Taylor P, Südhof TC. A splice code for trans-synaptic cell adhesion mediated by binding of neuroligin 1 to alpha- and beta-neurexins. *Neuron*. 2005; 48:229–236. [PubMed: 16242404]
- Boucard AA, Ko J, Südhof TC. High-affinity neurexin binding to the cell-adhesion G-protein coupled receptor CIRL1/Latrophilin-1 produces an intercellular adhesion complex. *J Biol Chem*. 2012; 287:9399–9413. [PubMed: 22262843]
- Chen K, Gracheva EO, Yu SC, Sheng Q, Richmond J, Featherstone DE. Neurexin in embryonic *Drosophila* neuromuscular junctions. *PLoS One*. 2010; 5:e11115. [PubMed: 20559439]
- Chih B, Gollan L, Scheiffle P. Alternative splicing controls selective trans-synaptic interactions of the neuroligin-neurexin complex. *Neuron*. 2006; 51:171–178. [PubMed: 16846852]
- de Wit J, Sylwestrak E, O'Sullivan ML, Otto S, Tiglio K, Savas JN, Yates JR 3rd, Comoletti D, Taylor P, Ghosh A. LRRTM2 interacts with Neurexin 1 and regulates excitatory synapse formation. *Neuron*. 2009; 64:799–806. [PubMed: 20064388]
- Etherton MR, Blaiss C, Powell CM, Südhof TC. Mouse neurexin-1 α deletion causes correlated electrophysiological and behavioral changes consistent with cognitive impairments. *Proc Natl Acad Sci USA*. 2009; 106:17998–18003. [PubMed: 19822762]
- Fuccillo MV, Földy C, Gökce O, Rothwell PE, Sun G, Malenka RC, Südhof TC. Single-Cell mRNA Profiling Reveals Cell-Type Specific Expression of Neurexin Isoforms. *Neuron*. 2015; 87:326–340. [PubMed: 26182417]
- Ganot P, Zoccola D, Tambutté E, Voolstra CR, Aranda M, Allemand D, Tambutté S. Structural molecular components of septate junctions in cnidarians point to the origin of epithelial junctions in eukaryotes. *Mol Biol Evol*. 2015; 32:44–62. [PubMed: 25246700]
- Guo L, Xiong H, Kim J-I, Wu Y-W, Lalchandani RR, Cui Y, et al. Dynamic rewiring of neural circuits in the motor cortex in mouse models of Parkinson's disease. *Nat Neurosci*. 2015; 18:1299–1309. [PubMed: 26237365]
- Hashimoto K, Kano M. Functional differentiation of multiple climbing fiber inputs during synapse elimination in the developing cerebellum. *Neuron*. 2003; 38:785–796. [PubMed: 12797962]
- Hashimoto K, Ichikawa R, Kitamura K, Watanabe M, Kano M. Translocation of a “winner” climbing fiber to the Purkinje cell dendrite and subsequent elimination of “losers” from the soma in developing cerebellum. *Neuron*. 2009; 63:106–118. [PubMed: 19607796]
- Ichtchenko K, Hata Y, Nguyen T, Ullrich B, Missler M, Moomaw C, Südhof TC. Neuroligin 1: a splice site-specific ligand for β -neurexins. *Cell*. 1995; 81:435–443. [PubMed: 7736595]
- Jiang M, Yang M, Yin L, Zhang X, Shu Y. Developmental reduction of asynchronous GABA release from neocortical fast-spiking neurons. *Cereb Cortex*. 2015; 25:258–270. [PubMed: 23968835]
- Kaaser PS, Deng L, Wang Y, Dulubova I, Liu X, Rizo J, Südhof TC. RIM proteins tether Ca^{2+} -channels to presynaptic active zones via a direct PDZ-domain interaction. *Cell*. 2011; 144:282–295. [PubMed: 21241895]
- Ko J, Fuccillo MV, Malenka RC, Südhof TC. LRRTM2 functions as a neurexin ligand in promoting excitatory synapse formation. *Neuron*. 2009; 64:791–798. [PubMed: 20064387]
- Li J, Ashley J, Budnik V, Bhat MA. Crucial role of *Drosophila* neurexin in proper active zone apposition to postsynaptic densities, synaptic growth, and synaptic transmission. *Neuron*. 2007; 55:741–755. [PubMed: 17785181]
- Lorenzetto E, Caselli L, Feng G, Yuan W, Nerbonne JM, Sanes JR, Buffelli M. Genetic perturbation of postsynaptic activity regulates synapse elimination in developing cerebellum. *Proc Natl Acad Sci USA*. 2009; 106:16475–16480. [PubMed: 19805323]
- Maro GS, Gao S, Olechwier AM, Hung WL, Liu M, Özkan E, Zhen M, Shen K. MADD-4/Punctin and Neurexin Organize *C. elegans* GABAergic Postsynapses through Neuroligin. *Neuron*. 2015; 86:1420–1432. [PubMed: 26028574]
- Matsuda K, Yuzaki M. Cbln family proteins promote synapse formation by regulating distinct neurexin signaling pathways in various brain regions. *Eur J Neurosci*. 2011; 33:1447–1461. [PubMed: 21410790]
- Missler M, Hammer RE, Südhof TC. Neurexophilin binding to α -neurexins: A single LNS-domain functions as independently folding ligand-binding unit. *J Biol Chem*. 1998; 273:34716–34723. [PubMed: 9856994]

- Missler M, Zhang W, Rohlmann A, Kattenstroth G, Hammer RE, Gottmann K, Südhof TC. α -Neurexins couple Ca^{2+} channels to synaptic vesicle exocytosis. *Nature*. 2003; 423:939–948. [PubMed: 12827191]
- Owald D, Khorramshahi O, Gupta VK, Banovic D, Depner H, Fouquet W, Wichmann C, Mertel S, Eimer S, Reynolds E, Holt M, Aberle H, Sigrist SJ. Cooperation of Syd-1 with Neurexin synchronizes pre- with postsynaptic assembly. *Nat Neurosci*. 2012; 15:1219–1226. [PubMed: 22864612]
- Petrenko AG, Ullrich B, Missler M, Krasnoperov V, Rosahl TW, Südhof TC. Structure and evolution of neurexophilin. *J Neurosci*. 1996; 16:4360–4369. [PubMed: 8699246]
- Schreiner D, Nguyen TM, Russo G, Heber S, Patrignani A, Ahrné E, Scheiffele P. Targeted combinatorial alternative splicing generates brain region-specific repertoires of neurexins. *Neuron*. 2014; 84:386–98. [PubMed: 25284007]
- Siddiqui TJ, Pancaroglu R, Kang Y, Rooyackers A, Craig AM. LRRTMs and neuroligins bind neurexins with a differential code to cooperate in glutamate synapse development. *J Neurosci*. 2010; 30:7495–7506. [PubMed: 20519524]
- Sugita S, Saito F, Tang J, Satz J, Campbell K, Südhof TC. A stoichiometric complex of neurexins and dystroglycan in brain. *J Cell Biol*. 2001; 154:435–445. [PubMed: 11470830]
- Tabuchi K, Südhof TC. Structure and evolution of the neurexin genes: Insight into the mechanism of alternative splicing. *Genomics*. 2002; 79:849–859. [PubMed: 12036300]
- Treutlein B, Gokce O, Quake SR, Südhof TC. Cartography of neurexin alternative splicing mapped by single-molecule long-read mRNA sequencing. *Proc Natl Acad Sci USA*. 2014; 111:E1291–1299. [PubMed: 24639501]
- Uemura T, Lee SJ, Yasumura M, Takeuchi T, Yoshida T, Ra M, Taguchi R, Sakimura K, Mishina M. Trans-synaptic interaction of GluRdelta2 and neurexin through Cbln1 mediates synapse formation in the cerebellum. *Cell*. 2010; 141:1068–1079. [PubMed: 20537373]
- Ullrich B, Ushkaryov YA, Südhof TC. Cartography of neurexins: more than 1000 isoforms generated by alternative splicing and expressed in distinct subsets of neurons. *Neuron*. 1995; 14:497–507. [PubMed: 7695896]
- Ushkaryov YA, Petrenko AG, Geppert M, Südhof TC. Neurexins: Synaptic cell surface proteins related to the α -latrotoxin receptor and laminin. *Science*. 1992; 257:50–56. [PubMed: 1621094]
- Ushkaryov YA, Südhof TC. Neurexin III α : Extensive alternative splicing generates membrane-bound and soluble forms in a novel neurexin. *Proc Natl Acad Sci USA*. 1993; 90:6410–6414. [PubMed: 8341647]
- Ushkaryov YA, Hata Y, Ichtchenko K, Moomaw C, Afendis S, Slaughter CA, Südhof TC. Conserved domain structure of β -Neurexins. *J Biol Chem*. 1994; 269:11987–11992. [PubMed: 8163501]
- Wadiche JI, Jahr CE. Multivesicular release at climbing fiber-Purkinje cell synapses. *Neuron*. 2001; 32:301–313. [PubMed: 11683999]
- Xu W, Südhof TC. A neural circuit for memory specificity and generalization. *Science*. 2013; 339:1290–1295. [PubMed: 23493706]
- Zhang B, Chen LY, Liu X, Maxeiner S, Lee SJ, Gokce O, Südhof TC. Neuroligins sculpt cerebellar Purkinje-cell circuits by differential control of distinct classes of synapses. *Neuron*. 2015; 87:781–796. [PubMed: 26291161]

Highlights

- Pan-neurexin KO causes diverse synaptic phenotypes in a synapse-specific manner
- Neurexin-deficiency phenotypes range from synapse numbers to synaptic Ca^{2+} -dynamics
- Phenotypes in neurexin-deficient synapses confirm organizer function of neurexins
- Diversity of pan-neurexin KO phenotypes argues against canonical neurexin functions

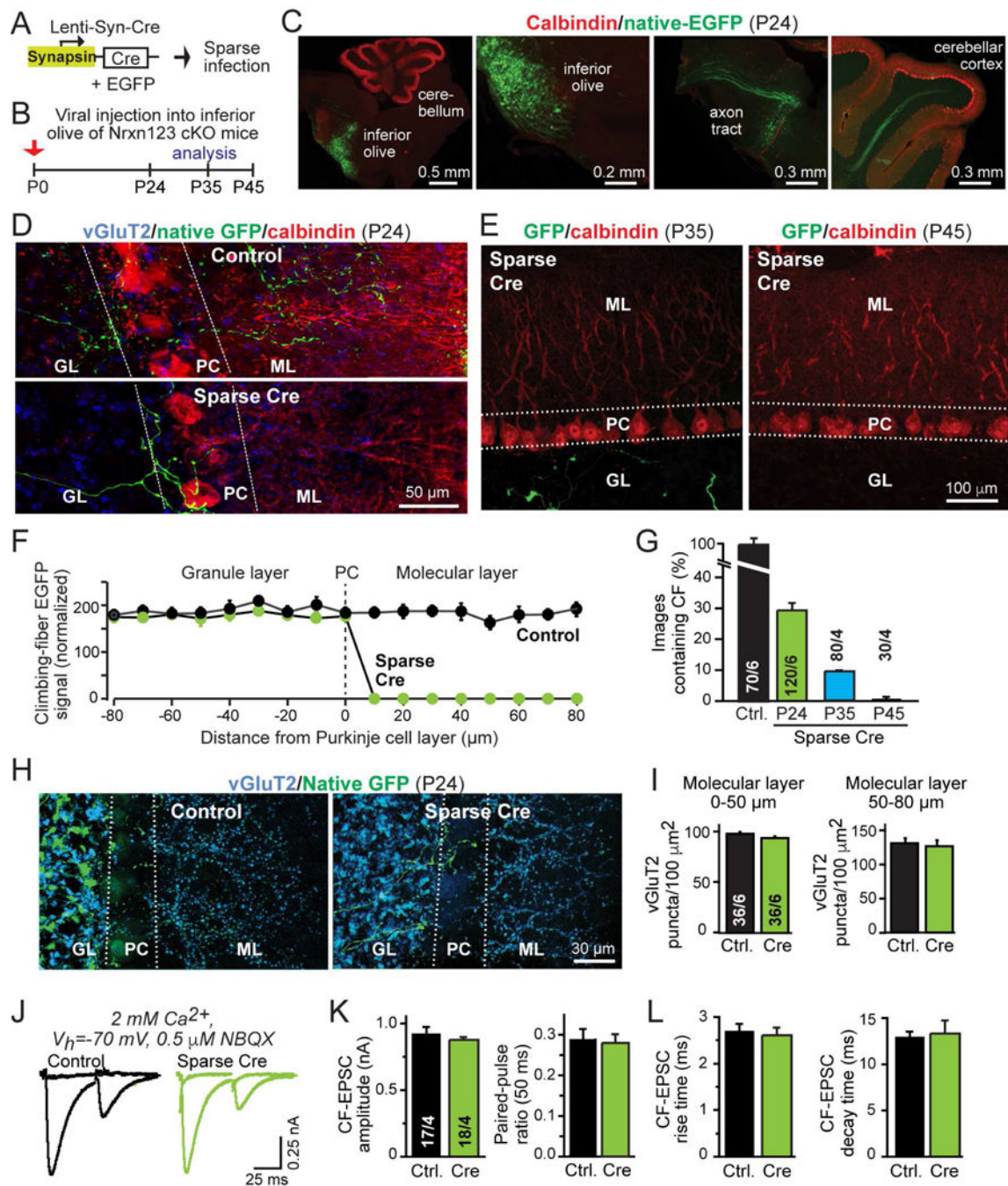


Figure 1. Sparse deletion of all neurexins in the inferior olive causes retraction of presynaptic climbing fibers from the cerebellar cortex

(A) Schematic of lentiviruses used for sparse deletion of presynaptic neurexins from inferior olive neurons in Nrnx123 cKO mice.

(B) Timeline of experiments, with stereotaxic injections of lentiviruses at P0, and analysis at P24, P35, or P45. Test mice were co-infected with viruses encoding Cre-recombinase and double-floxed EGFP; control mice were infected with virus expressing mVenus (an EGFP derivative) and inactive Cre-recombinase (Cre).

(C) Representative images of sagittal brain sections with sparse viral infection of the inferior olive in *Nrxn123* cKO mice, stained for calbindin (red) and imaged additionally for co-expressed EGFP (green). Images show the inferior olive injection site (left two panels), and EGFP-expressing climbing fibers extending from the brain stem (middle right panel) and entering the cerebellar cortex (right panel). Injection site and axon projections were visualized in different sections from the same brain.

(D) Representative confocal images of cerebellar cortex sections after sparse infection of the inferior olive of *Nrxn123* cKO mice with Cre-expressing or control viruses at P0, and analysis at P24 (green, EGFP-positive climbing fibers; red, calbindin; blue, vGluT2; GL, granule cell layer; PC, Purkinje cell layer; ML, molecular layer).

(E) Same as D, except that sections were obtained at P35 and P45, and no vGluT2 labeling was performed. Injection sites were confirmed in each animal (see Fig. S3).

(F) Plot of the climbing-fiber EGFP fluorescence intensity measured across the cerebellar cortex after in mice at P24 after sparse inferior olive infection at P0 with control viruses or viruses deleting all neurexins. Dashed line corresponds to the entire Purkinje cell layer as outlined by dashed lines in D; EGFP fluorescence was quantified as a function of the distance from these lines as indicated on the X-axis. Fluorescence intensity (arbitrary units) was averaged and normalized to background fluorescence.

(G) Summary graph of the percentage of cerebellar sections containing EGFP-positive climbing fibers in sections from control injected and Cre-injected mice at P24, and from Cre-injected mice at P35 and P45. Regions of interest ($100 \mu\text{m}^2$) were randomly selected from granule cell layers in cerebellar lobule IV and V.

(H) Representative images of cerebellar cortex sections as in D, imaged for vGluT2 (blue) and EGFP to visualize total climbing-fiber synapse density.

(I) Summary graphs of the density of vGluT2⁺ synaptic puncta in the molecular layer proximal (0–50 μm , left) or distal to the Purkinje cell layer (50–80 μm , right) in cerebella obtained as in D.

(J–L) Normal electrophysiological properties of climbing-fiber synapses after sparse presynaptic deletion of neurexins (J, representative traces of climbing-fiber EPSCs elicited by consecutive stimuli separated by 50 ms [flat lines are below-threshold stimulations to illustrate all-or-none response nature]; K, summary graphs of the EPSC amplitude and paired-pulse ratio; L, summary graphs of the EPSC rise and decay times).

Data in summary graphs are means \pm SEM; statistical comparisons were performed with Student's t-test (* $P < 0.05$; ** $P < 0.01$; *** $P < 0.001$; non-significant comparisons are not labeled). Numbers in bars indicate the number of sections/mice (G & I) or cells/mice (K & L) examined. For additional data, see Fig. S1–3.

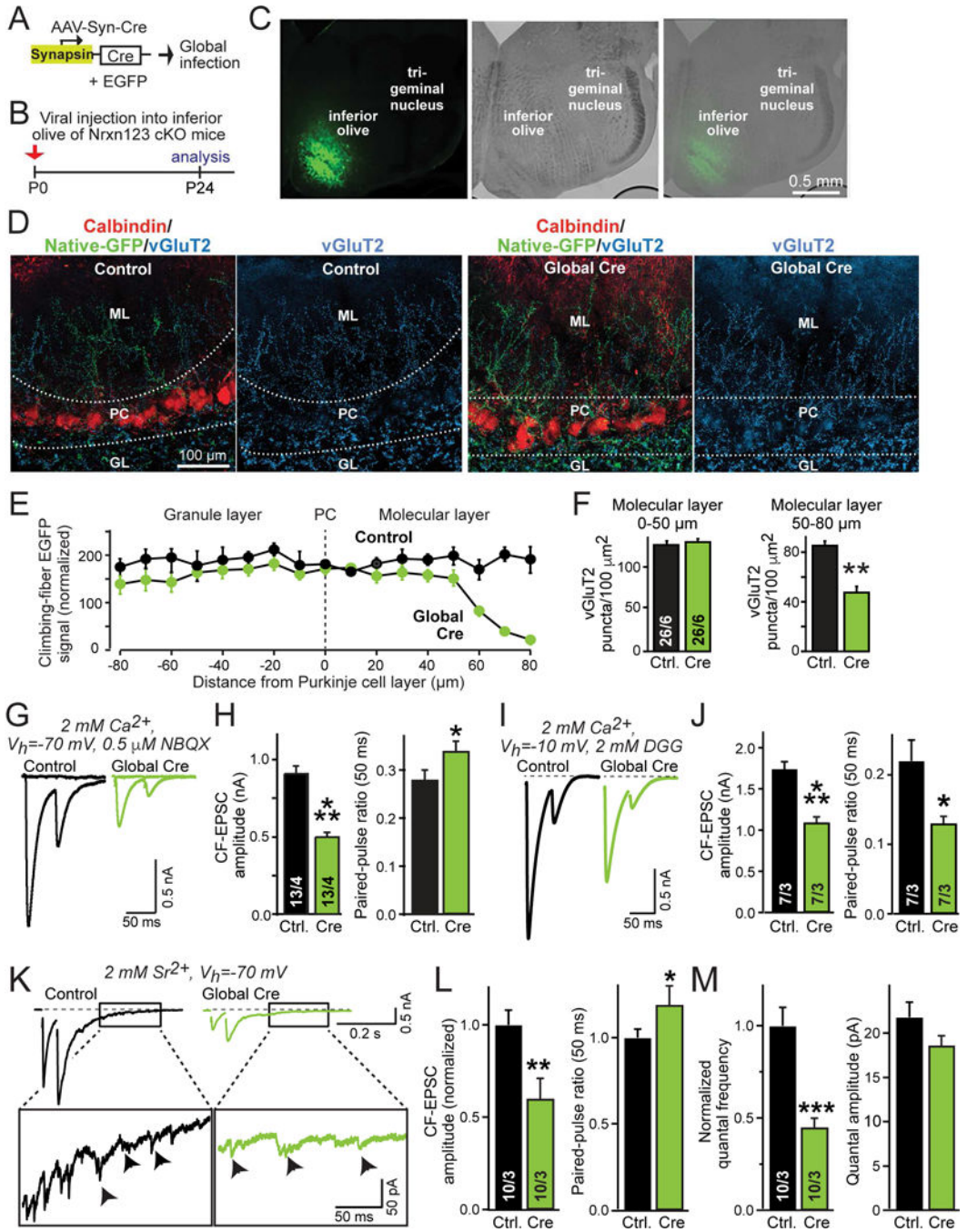


Figure 2. Global pan-neurexin deletions in the inferior olive impair presynaptic climbing-fiber synaptic transmission

(A) Schematic of AAVs used for global deletion of presynaptic neurexins in inferior olive neurons of *Nrxn123* cKO mice.

(B) Schedule of experiments, with stereotactic injections at P0, and analysis at P24, using the AAV equivalents of the test and control viruses described in Fig. 1.

(C) Representative fluorescence (left) and DIC (differential interference contrast, middle) images of the inferior olive at P24 (right) after stereotactic infection with AAVs at P0.

(D) Representative confocal images of cerebellar cortex sections obtained from mice after global infection of the inferior olive with AAVs expressing mutant or active Cre-recombinases. Left, sections were stained for calbindin (red) and vGluT2 (blue), with GFP⁺-climbing fibers visualized in green; right, sections were stained for vGluT2.

(E) Plot of the climbing-fiber EGFP fluorescence intensity measured across the cerebellar cortex after in mice at P24 after global inferior olive infection at P0 with control viruses or viruses deleting all neurexins. Dashed vertical line corresponds to the entire Purkinje cell layer as outlined by dashed lines in D; EGFP fluorescence was quantified as a function of the distance from these lines as indicated on the X-axis. Fluorescence intensity (arbitrary units) was averaged and normalized to background fluorescence.

(F) Summary graphs of the density of vGluT2⁺ synaptic puncta in the molecular layer proximal (0–50 μm, left) or distal to the Purkinje cell layer (50–80 μm, right) in cerebella obtained as in D.

(G & H) Impaired electrophysiological properties of climbing-fiber synapses after global presynaptic deletion of neurexins (G, representative traces of climbing-fiber EPSCs elicited by consecutive stimuli separated by 50 ms; H, summary graphs of EPSC amplitudes and paired-pulse ratio).

(I & J) Climbing-fiber EPSCs recorded at a holding potential of –10 mV in the presence of the low-affinity competitive AMPA-receptor antagonist γ -D-glutamylglycine (DGG; 2 mM; included in the medium; I, representative traces of climbing fiber EPSCs; J, summary plots of the EPSC amplitude and paired-pulse ratio).

(K–M) Climbing-fiber EPSCs recorded in Sr²⁺ (2 mM) instead of Ca²⁺ reveal that the size and properties of climbing-fiber quantal events are normal, even though synaptic transmission is impaired. K, representative traces; L, summary graphs of the evoked climbing-fiber EPSC amplitude and paired-pulse ratio; M, summary graphs of the frequency and amplitude of quantal events of climbing fiber synapses monitored 170–370 ms after the peak of the second EPSC. Cerebellar slices were examined at P35–P40 after P0 global viral infections.

Data in summary graphs are means \pm SEM; statistical comparisons were performed with Student's t-test (*P<0.05; **P<0.01; ***P<0.001; non-significant comparisons are not labeled). Numbers in bars indicate the number of sections/mice (F) or cells/mice (H, J, L & M) examined. Abbreviations: GL, granule layer; PC, Purkinje cell layer; ML, molecular layer. For additional data, see Fig. S4.

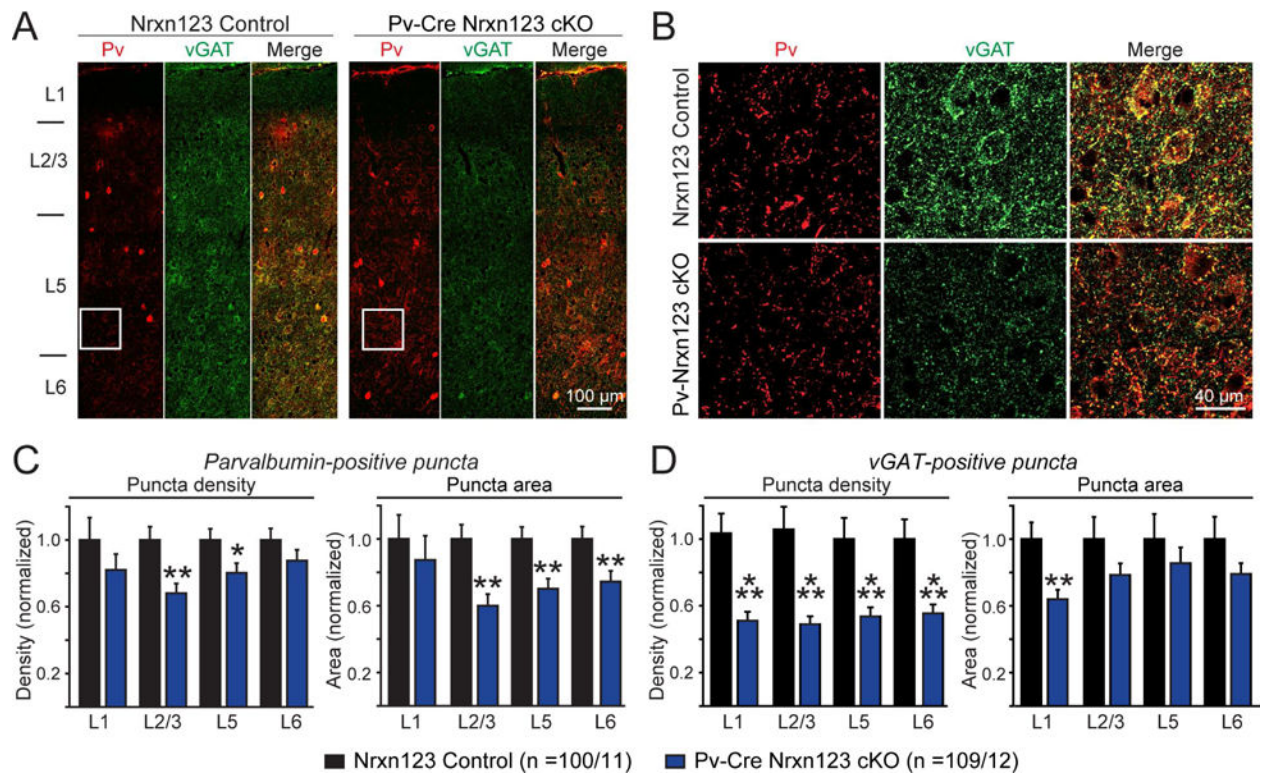


Figure 3. Pv-Cre mediated deletion of all neuexins in parvalbumin-positive (Pv^+) interneurons decreases the density of Pv^+ inhibitory synapses in the medial prefrontal cortex (mPFC)
(A) Representative images (assembled from multiple overlapping views) of mPFC sections that were immunostained for parvalbumin (red) and the vesicular GABA transporter (vGAT, green). Sections were from littermate control Nrnx123 cKO (left) and Pv-Cre Nrnx123 cKO mice (right). Cortical layers L1 to L6 are indicated on the left.
(B) Expansion of the image sections boxed in A.
(C, D) Summary graphs of the density (left) and apparent area (right) of Pv^+ (C) and vGAT⁺ synaptic puncta (D) quantified separately for each cortical layer.
 Data in summary graphs are means \pm SEM; statistical comparisons were performed with Student's t-test (* $P < 0.05$; ** $P < 0.01$; *** $P < 0.001$; non-significant comparisons are not labeled). Numbers indicate the number of mPFC sections and mice examined. For additional data, see Fig. S6.

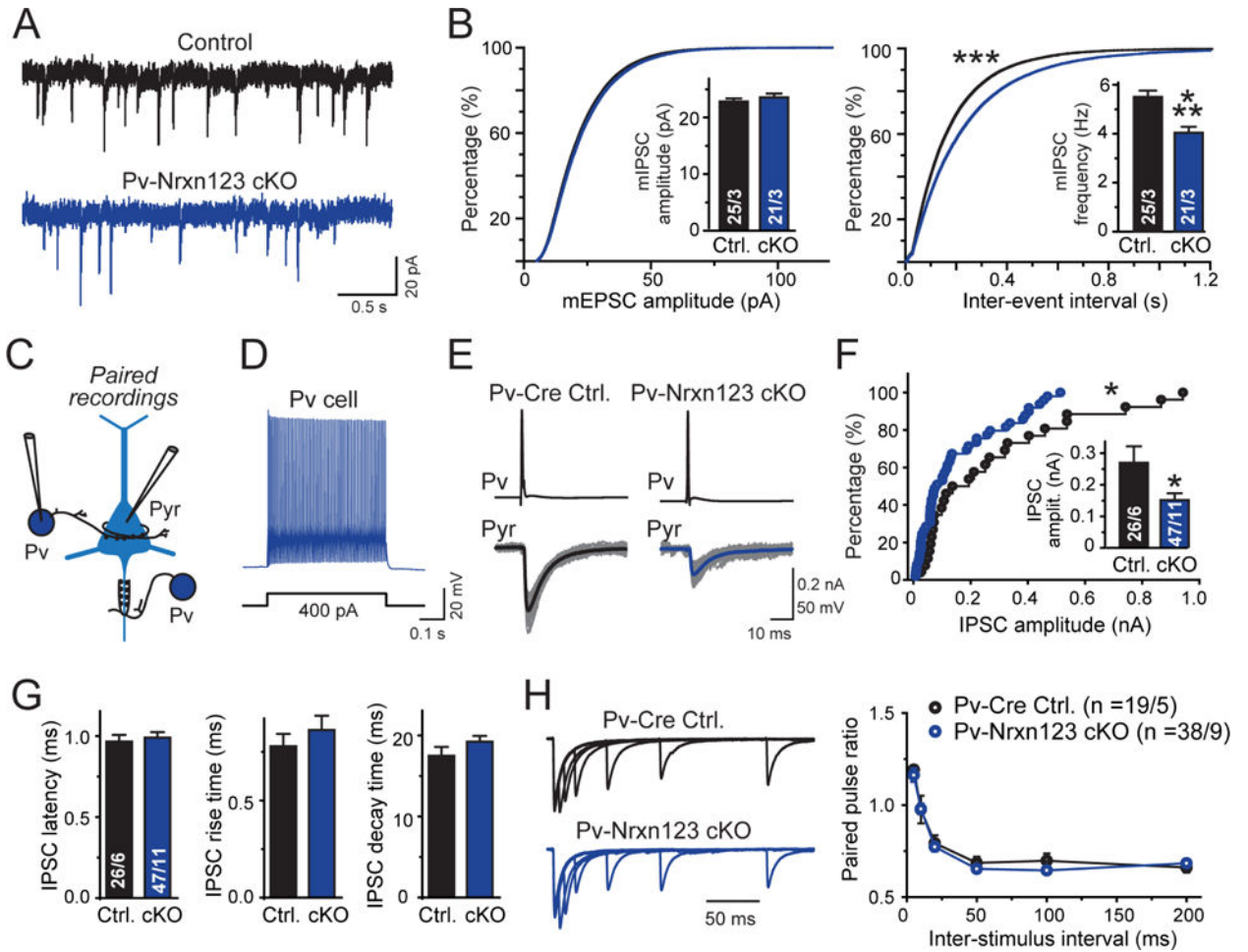


Figure 4. Paired recordings reveal that Pv-Cre mediated deletion of all neurexins in Pv⁺ interneurons decreases inhibitory synaptic transmission at pyramidal neuron synapses of the mPFC similar to the synapse density

(A) Representative mIPSC traces recorded from mPFC layer 5 pyramidal neurons in acute mPFC slices from littermate control Nrxn123 cKO and Pv-Cre Nrxn123 cKO cells.

(B) Cumulative distribution plots of mIPSC amplitudes (left) and inter-event intervals (right) monitored in pyramidal neurons of Nrxn123 cKO and Pv-Cre Nrxn123 cKO mice (insets = summary graphs of average mIPSC amplitude (left) and frequency (right)).

(C) Diagram of paired recording to monitor inhibitory synapses formed by Pv⁺ interneurons on the perisomatic region and axon initial segments of pyramidal neurons (Pyr). For all recordings of interneuron-pyramidal neuron pairs, the necessity of visual identification of interneurons (mediated by viral injections of AAV-EF1 α -DIO-eYFP) required that controls were from non-littermate Pv-Cre mice with a similar genetic background.

(D) Representative traces of a typical fast-spiking firing pattern of Pv⁺ interneurons.

(E) Representative traces showing unitary synaptic connections between a Pv⁺ interneuron and a pyramidal neuron in Pv-Cre control and Pv-Nrxn123 cKO mice (grey traces, overlaid individual responses from different trials; black/blue traces, averaged responses).

(F) Cumulative probability plot of unitary mean IPSC amplitudes (inset = summary graph of IPSC amplitudes) showing that Pv-Cre Nr1h3 cKO neurons exhibit a decrease in synaptic strength.

(G) Summary plots of the latency (left), rise time (center), and decay time (right) of unitary IPSCs in Pv-interneuron → pyramidal neuron synapses.

(H) Representative traces of paired pulse ratios (PPRs) of unitary IPSCs in Pv-interneuron → pyramidal neuron synapses at different interstimulus intervals (left), and summary graph of PPRs as a function of the inter-stimulus interval (right).

Data in summary graphs are means \pm SEM; statistical comparisons were performed with Student's t-test (* $P < 0.05$; ** $P < 0.01$; *** $P < 0.001$; non-significant comparisons are not labeled). Numbers indicate the number of connected cell pairs/mice examined. For additional data, see Fig. S6.

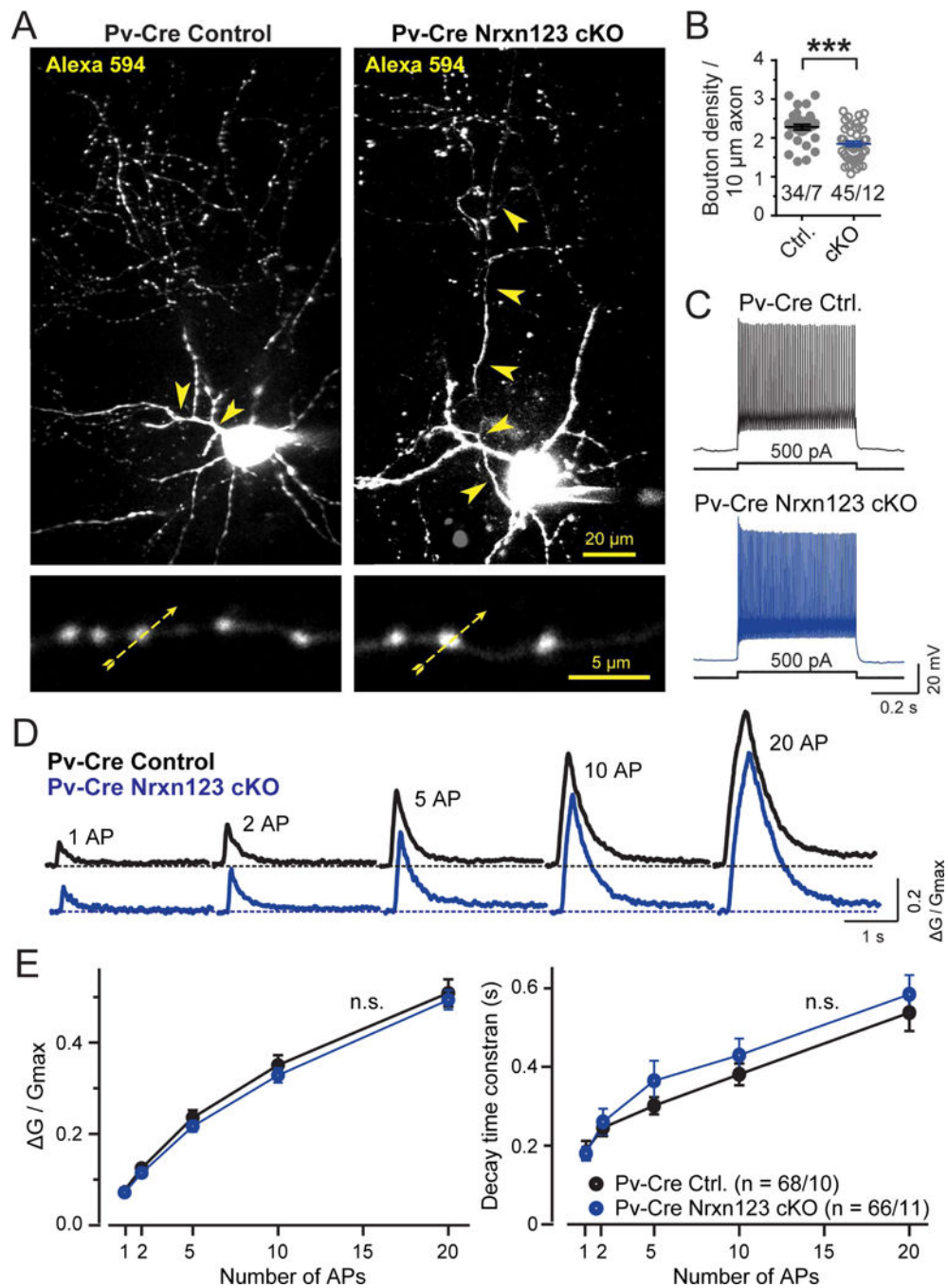


Figure 5. Two-photon microscopy reveals that Pv-Cre mediated pan-neurexin deletion in Pv^+ interneurons does not alter action potential-induced Ca^{2+} -influx into presynaptic terminals, but decreases the density of presynaptic axonal boutons

(A) Pv^+ interneurons visualized by Alexa Fluor 594 fluorescence in Pv-Cre control and in Pv-Cre Nrnx123 cKO mice. Neurons identified via virally administered double-floxed mCherry were filled via the patch pipette with Alexa Fluor 594 (50 μ M; to visualize the axonal arbor and dendrites) and Fluo-5F (200 μ M; to monitor presynaptic Ca^{2+} -transients). The top image depicts a representative z-stack projection of the entire neuron (arrowheads =

axon). The bottom image displays an expanded view of axonal boutons (yellow dashed arrows = line scans during action potential stimulation).

(B) Decreased density of axonal boutons of neurexin-deficient Pv^+ interneurons (circles, individual axon branches; lines, means \pm SEM).

(C) Representative traces depicting the fast-spiking firing pattern of Pv^+ interneurons in Pv -Cre and Pv -Cre $Nrxn123$ cKO interneurons.

(D) Representative traces of Ca^{2+} -transients monitored via Fluo-5F fluorescence in presynaptic boutons by line scans as indicated in A. Trains of action potentials (1, 2, 5, 10, 20 APs at 50 Hz) were elicited by injecting current pulses (2 nA, 1 ms) via the recording pipettes.

(E) Summary plots of the peak amplitudes (G/G_{max} , *left*) and decay times (measured from 100% to 37% of peak amplitude, *right*) of Ca^{2+} -transients as a function of action potential number monitored in presynaptic boutons of Pv^+ interneurons.

Data in B and E are means \pm SEM (numbers indicate number of axon branches/neurons analyzed [B] or boutons/neurons analyzed [E]); statistical comparisons were performed with Student's t-test (* $P < 0.05$; ** $P < 0.01$; *** $P < 0.001$); non-significant comparisons are not labeled.

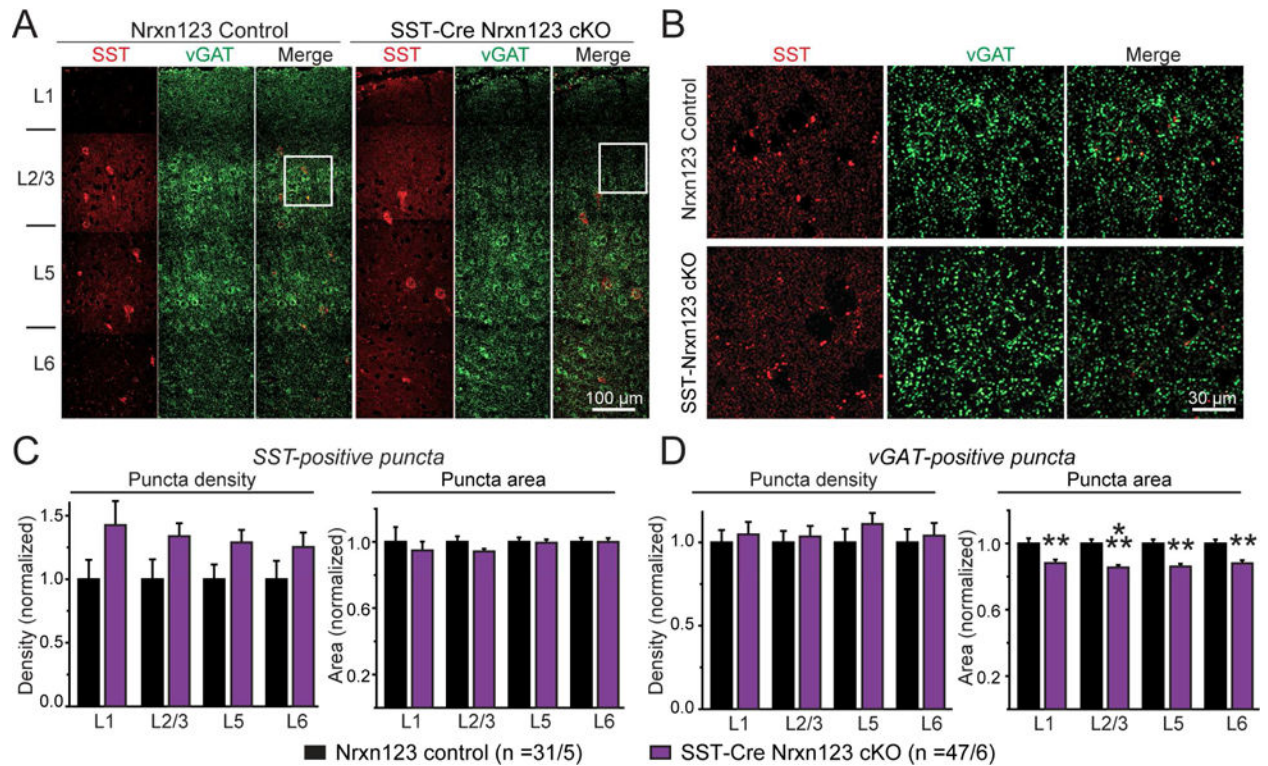


Figure 6. SST-Cre mediated pan-neurexin deletion in somatostatin-positive (SST⁺) interneurons induces minor changes in synapse numbers in the mPFC

(A) Representative images (assembled from multiple overlapping views) of mPFC sections that were immunostained for SST (red) and the vesicular GABA transporter (vGAT, green). Sections were from littermate control Nrxn123 cKO (left) and SST-Cre Nrxn123 cKO mice (right). Cortical layers L1 to L6 are indicated on the left.

(B) Expansion of the boxed sections outlined in A.

(C, D) Summary graphs of the density (left) and apparent area (right) of SST⁺ (C) and vGAT⁺ synaptic puncta (D) quantified separately in each cortical layer.

Data in summary graphs are means \pm SEM; statistical comparisons were performed with Student's t-test (* $P < 0.05$; ** $P < 0.01$; *** $P < 0.001$; non-significant comparisons are not labeled). Numbers indicate the number of mPFC sections and mice examined. For additional data, see Fig. S7.

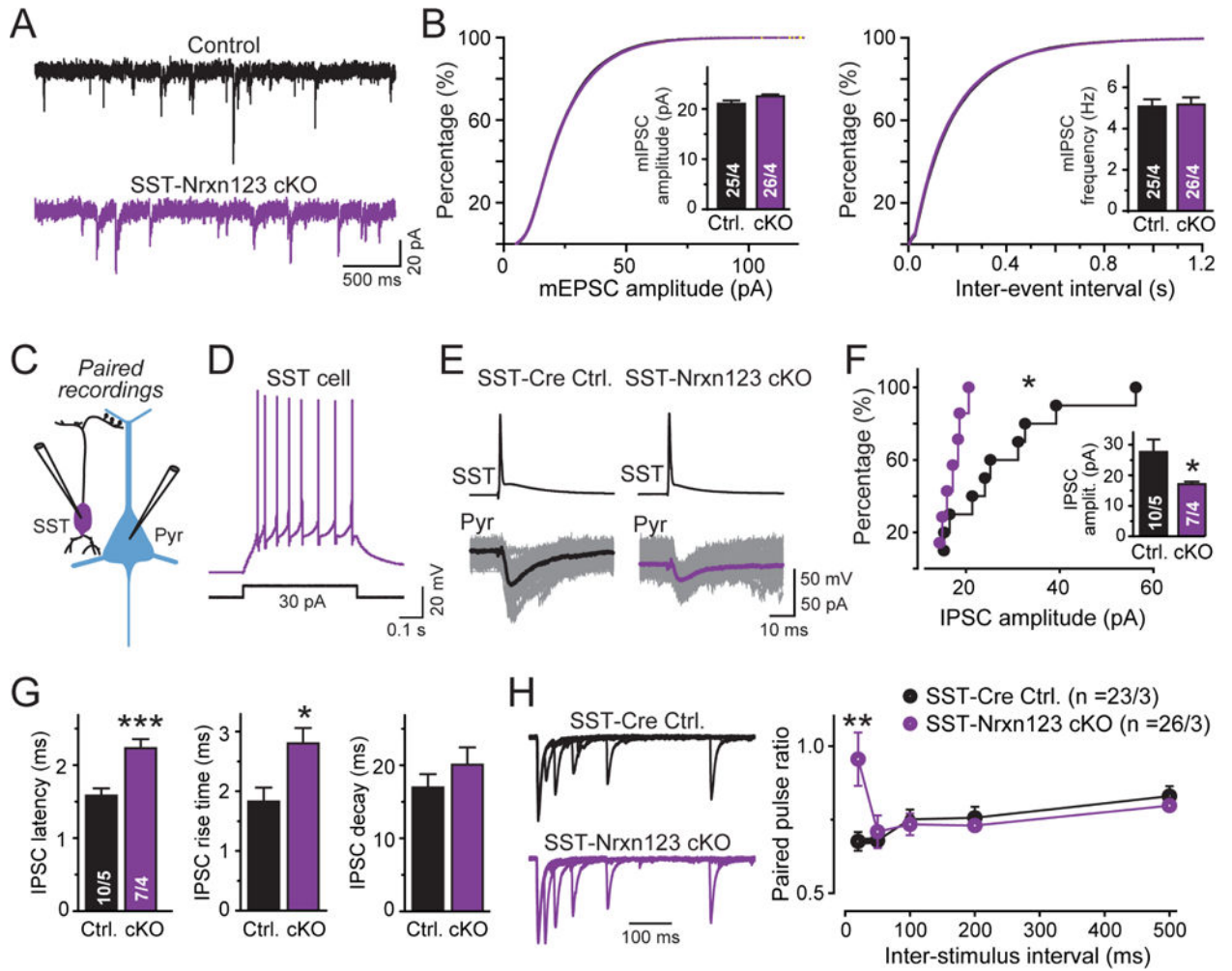


Figure 7. SST-Cre mediated pan-neurexin deletion in SST⁺ interneurons impairs evoked synaptic transmission as monitored by paired recordings and optogenetics

(A) Representative mIPSC traces from littermate Nrxn123 cKO control and SST-Cre Nrxn123 cKO pyramidal neurons.

(B) Cumulative probability plots of the mIPSC amplitudes (left) and inter-event intervals (right); insets show summary graphs of the mean mIPSC amplitude (left) and frequency (right).

(C) Paired recording configuration to monitor inhibitory synapses formed by SST⁺ interneurons on the distal dendrites of a pyramidal neuron (Pyr). For all recordings of interneuron-pyramidal neuron pairs, the necessity of visual identification of interneurons (mediated by viral injections of AAV-EF1 α -DIO-eYFP) required that controls are from non-littermate SST-Cre mice with a similar genetic background.

(D) Representative traces of a typical low-threshold-spike firing pattern of SST⁺ interneurons.

(E) Representative paired-recording traces showing unitary synaptic connections between an SST⁺ interneuron and a pyramidal neuron in SST-Cre control or SST-Nrxn123 cKO mice. SST⁺ cells were identified in slices by eYFP fluorescence after infection with AAVs containing double-floxed eYFP expression cassettes. IPSCs were evoked by current

injections into patched presynaptic SST⁺ interneurons (top), and recorded from patched postsynaptic pyramidal neurons (bottom grey traces, overlaid individual responses; black/purple traces, averaged responses).

(F) Cumulative probability plot of unitary mean IPSC amplitudes (inset = summary graph of IPSC amplitudes) showing that in the overall cell population, the synaptic strength is preferentially decreased in neurons with high IPSC amplitudes.

(G) Summary plots of latency (left), rise time (center), and decay time (right) of unitary IPSCs in SST-interneuron → pyramidal neuron synapses.

(H) Representative traces of paired pulse ratios (PPRs) of unitary IPSCs in SST-interneuron → pyramidal neuron synapses at increasing interstimulus intervals (left), and summary graph of the mean PPRs as a function of the inter-stimulus interval (right). Unitary IPSCs were evoked by optogenetic stimulation of SST⁺ cells after stereotactic infection of the mice with AAVs encoding CAG-DIO-ChR2-tdTomato.

Data in summary graphs are means ± SEM; statistical comparisons were performed with Student's t-test (*P<0.05; **P<0.01; ***P<0.001; non-significant comparisons are not labeled). Numbers indicate the number of cells and mice examined. For additional data, see Fig. S7.

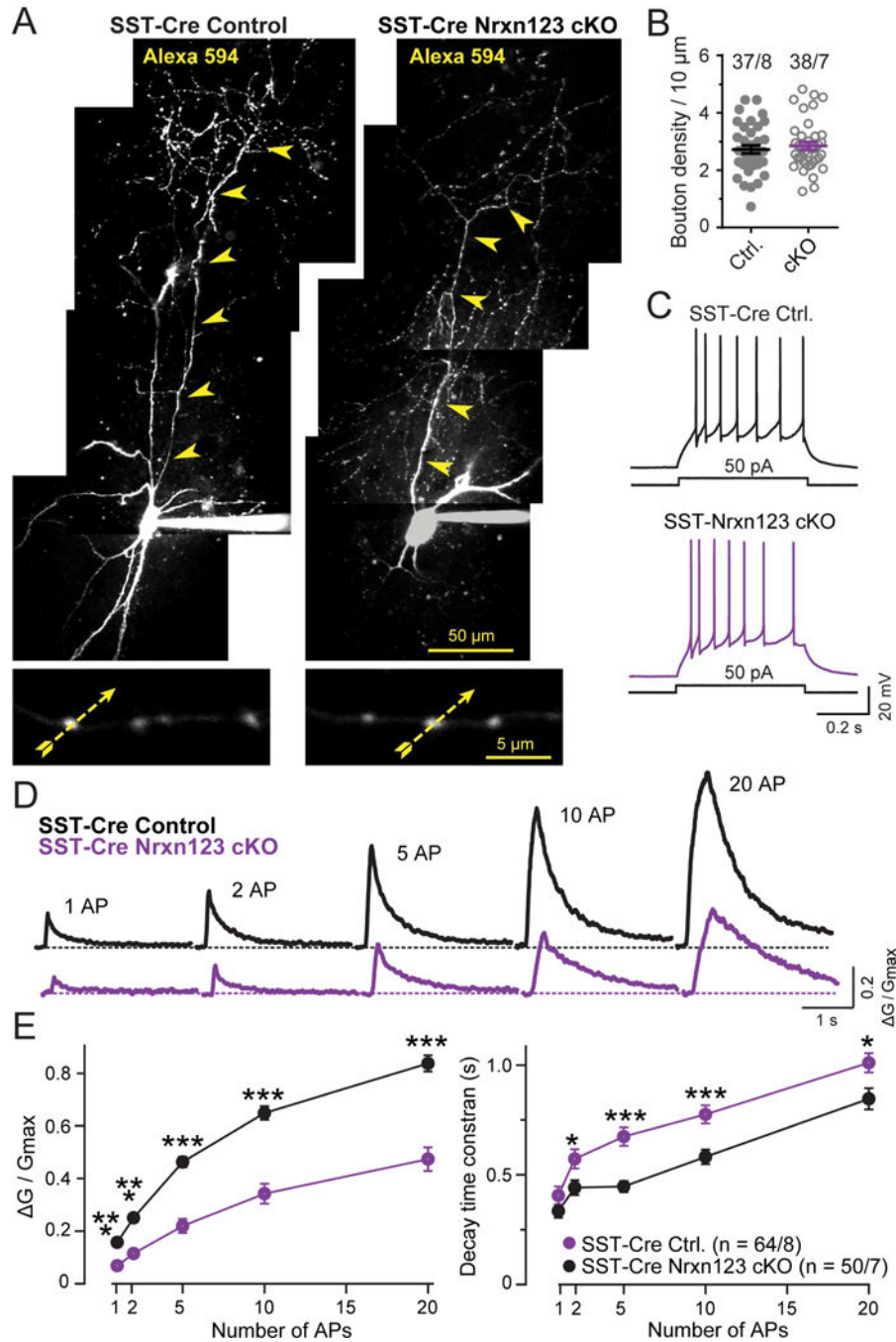


Figure 8. Two-photon microscopy reveals that SST-Cre mediated pan-neurexin deletion in somatostatin-positive (SST⁺) interneurons dramatically decreased action potential-evoked presynaptic Ca²⁺-transients in SST⁺ interneurons

(A) Morphology of SST⁺ interneurons visualized by Alexa Fluor 594 fluorescence in control SST-Cre and in SST-Cre Nrnx123 cKO mice. Neurons identified via virally administered double-floxed eYFP were filled via the patch pipette with Alexa Fluor 594 (50 mM; to visualize the axonal arbor) and Fluo-5F (200 μ M; to monitor presynaptic Ca²⁺-transients). The top image depicts a representative z-stack projection of the entire neuron (arrowheads = axon). The bottom image displays an expanded view of axonal boutons (yellow dashed

arrows = line scans during action potential stimulation). Note that axons of SST⁺ interneurons extend into superficial mPFC layers (~ 500 μm away from the soma).

(B) Normal density of axonal boutons of neurexin-deficient SST⁺ interneurons (circles, individual cells; lines, means ± SEM).

(C) Representative traces depicting the low-threshold spiking firing pattern of SST⁺ interneurons in SST-Cre control and SST-Cre Nrnx123 cKO interneurons.

(D) Representative traces of Ca²⁺-transients monitored via Fluo-5F fluorescence in presynaptic boutons by line scans as indicated in A. Trains of APs (1, 2, 5, 10, 20 APs at 50 Hz) were elicited by injecting current pulses (2 nA, 1 ms) through recording pipettes.

(E) Summary plots of the peak amplitudes (G/G_{max} , left) and decay times (measured from 100% to 37% of peak amplitude, right) of Ca²⁺-transients as a function of action potential numbers monitored in presynaptic boutons from SST⁺ control and neurexin-deficient interneurons.

Data in B and E are means ± SEM (numbers indicate number of axon branches/neurons analyzed [B] or boutons/neurons analyzed [E]); statistical comparisons were performed with Student's t-test (*P<0.05; **P<0.01; ***P<0.001); non-significant comparisons are not labeled.

Assay Name	Gene name	Forward Primer	Probe	Reverse Primer
Actin	Actin Beta	AGGTCTTTACGGATGTCAACG	ATTCCATACCCAGAAGAAGGCTGG	ATTGGCAACGAGCGGTT
Syt1	Synaptotagmin 1	ATCATACACAGCCATCACACAG	AGGTGCCATACTCGGAATTAGGTGG	ACCCTCAATCCAGTCTTCAATG
Sst	Somatostatin	GGCATCATTTCTCTGCTGGTT	AGTTCCCTGTTCCCGGTGGCA	AGACTCCCGTCAGTTTCTCG
Gad2	Glutamate decarboxylase 2	GCCTTGTCTCTGTGTCAATAG	TGCATCAGTCCCTCCTCTCTAACCA	CCTTGCAGTGTTCAGTCT
Pv	Parvalbumin	CTTAGCTTTCAGCCACCAGAG	ATCTTGCCCGTCCCCATCCTTGTG	CTGTAAAGAAACAAAGACGCT
Syt2	Synaptotagmin 2	Mm.PT.51.12344265		
NRXN1-all	Neurexin 1	ACTACATCAGTAACCTAGCACAG	CTTCTCCTTGACCACAGCCCCAT	ACAAGTGTCCGTTTCAAATCTTG
NRXN1alpha	Neurexin 1 alpha	TCCTCTTAGACATGGGATCAGG	CAACGGGATGGACGGTCAAGTA	GTGTAGGGAGTGCCTAGTGTG
NRXN2alpha	Neurexin 2 alpha	GTCAGCAACAACCTTCATGGG	CTTCACTTTCGGGTCCCTTCTCT	AGCCACATCCTCACAAAG
NRXN3alpha	Neurexin 3 alpha	GGGAGAACCTGCGAAAGAG	CTGCCGTATAGCTCAGATAGATGC	ATGAAAGCGGAAAGGACACATC
CL1/Lphn1	Latrophilin 1	GACTGATGCTCTGACTCATGT	TGGGCACACGAAGATGTAAGGGAC	CTGGAAACCTACAAATACCTGGA
CL2/Lphn2	Latrophilin 2	CTCGTGGTGGATATTGTGGTT	TGACCTGCCCAAGTGCCTTAC	TTACGGTATTCCCTGGAGTTTG
LRRTM2	Leucine-rich repeat transmembrane protein 2	GGCCACTTGGAAATGTAAGCC	TGCAGCCTCCAATGTGCTCAGAA	C ACTGCGTTGAGTCTGACAAA
LRRTM3	Leucine-rich repeat transmembrane protein 3	CATATGCCAGAAAGGTTGACAC	AGGCTCCAGGGAATGTGAGATACCT	GAGATGCTGCTGAAACGGAA
LRRTM4	Leucine-rich repeat transmembrane protein 4	GAAATAGCACCCAGAAACACACTC	ACGGAAACCCATCCTTTTCTCATCCA	GACCAATAAAGAAGAAAGCTGAGAG
NL1	Neurologin 1	GGTTGGGTTTGGTATGGATGA	TGAGGAACTGGTTGATTTGGGTCACC	GATGTTGAGTGCAGTAGTAATGAC
NL1-ssA	Neurologin 1 splice site A out	CCAACTGAGATGATATTCGGG	GGGTCCCAAACCAAGTATGCTGT	CCAAAGACACTCCCACATACAG
Neurologin 2	Neurologin 2	CCGTGTAGAAAACAGCATGACC	TCAATCCGCCAGACACAGATATCCG	TGCTGTACCTCAAACCTCTA
Neurologin3	Neurologin 3	C ACTGTCTCGGATGCTTCA	CCTGTTTCTTAGCGCCGGATCCAT	CCTCTATCTGATGTGTATGTGC
Slitrk2	SLIT and NTRK-like protein 2	TCTTTAAGGACCTTCGATGTCA	CCGTCTTCTCTGATGTGTTTGCCT	GCTAAACTACTGGTGGACTGAA
Slitrk3	SLIT and NTRK-like protein 3	GGCTTTCATCATTCCTGGTTGA	TGGAGCGAACCTCGGAGATCCT	GACAGAATGACGGATACAATGC
Slitrk4	SLIT and NTRK-like protein 4	GTCACTGCCGACGAAGAG	TCCAGAGATAAAGCTGCTCAAAGACCG	CAGATCAAAGTAGAGAGGATCCG
Slitrk5	SLIT and NTRK-like protein 5	GGTCTGTTCCAAAGTTACTGG	ACGTGCATTTTACCCTCTGTTCCCATCT	TGGGTCCGGAGAAAGTTGC